

# High-Performance and Ultrafast Symmetric Supercapacitors Based on Cu(II)-Doped SrSnO<sub>3</sub> Perovskites

Adervando Silva, Mohamad Hasan Aleinawi, Emre Erdem, Brendan James Kennedy, Aurelian Catalin Galca, Iêda Maria Garcia dos Santos,\* Arpad Mihai Rostas,\* and André Luiz Menezes de Oliveira\*



Cite This: *J. Phys. Chem. C* 2025, 129, 15179–15195



Read Online

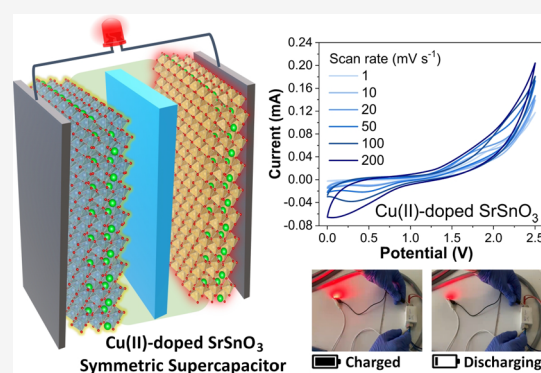
ACCESS |

Metrics & More

Article Recommendations

Supporting Information

**ABSTRACT:** Herein, Cu(II)-doped SrSnO<sub>3</sub> perovskites (SrSn<sub>1-x</sub>Cu<sub>x</sub>O<sub>3</sub>, namely SSO:Cu<sub>x</sub>) were prepared by a modified Pechini method and applied as supercapacitors (SCs) for the first time. The effect of dopant concentration ( $x = 1, 2.5,$  and  $5$  mol %) was investigated to fine-tune the structural and electronic properties to design potential candidates as SCs. The SSO:Cu<sub>x</sub> samples were characterized by conventional XRD and synchrotron XRD (S-XRD) combined with Rietveld refinements and spectroscopic analyses, such as Raman, FTIR, UV–vis, EPR, and XANES/NEXAFS. The electrochemical performance of the SSO:Cu<sub>x</sub> samples was investigated by cyclic voltammetry (CV), electrochemical impedance spectroscopy (EIS), and galvanostatic cycling with potential limitation (GCPL). It was evidenced that incorporating 2.5 mol % Cu(II) into the SrSnO<sub>3</sub> perovskite lattice (SrSn<sub>0.975</sub>Cu<sub>0.025</sub>O<sub>3</sub>, SSO:Cu2.5) led to a significant change in structural disorder and electronic properties, which play an essential role in creating a mixture of point defects such as reduced Sn<sup>3+</sup> and Cu<sup>+</sup> cations, and oxygen vacancies (V<sub>O</sub>). The SC device constructed with the SSO:Cu2.5 material showed a specific capacitance of 613 F g<sup>-1</sup> at a scan rate of 1 mV s<sup>-1</sup>, with a remarkable specific energy density and specific energy power of 25.42 W h kg<sup>-1</sup> and 32678.57 W kg<sup>-1</sup>, respectively, which are higher than those observed for any other available perovskite-based SCs. This performance was primarily attributed to the formation of mixed Sn<sup>4+</sup>/Sn<sup>3+</sup> and Cu<sup>2+</sup>/Cu<sup>+</sup> cations, which alter the structural and electronic properties of SrSnO<sub>3</sub>. Our findings indicate that an improved capability to store high energy and power may be achieved by fine-tuning the Cu(II) dopant concentration in the lattice and controlling the formation of undesired phases. This offers experimental guidance to design other Cu-doped perovskites as alternative materials for energy storage applications.



## INTRODUCTION

Limiting the use of fossil energy sources has attracted significant interest from the scientific community in technologies capable of generating and storing large amounts of clean and renewable energy,<sup>1</sup> such as batteries, fuel cells, and supercapacitors (SCs). Among these energy storage technologies, SCs are drawing attention and offer a unique combination of high energy density, fast charge, and discharge capabilities, in addition to having an exceptionally long lifetime by storing energy primarily within the double layer formed at the electrode–electrolyte interface (EEI).<sup>2</sup> These materials fall into three categories: electrical double-layer capacitors (EDLCs), pseudocapacitors (PCs), and hybrids.<sup>3</sup> In particular, PCs take advantage of reversible Faradaic redox processes in the EEI, employing materials with active redox sites, such as conducting polymers and transition metal oxides (TMOs).<sup>4</sup>

TMOs typically work as electrode materials in PCs because of their fast, reversible redox reactions, economy, and easy processability. Although PCs have a high power density, they are unsatisfactory in terms of power density and stability

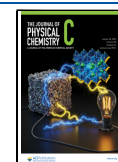
because of their low electrical conductivity and swelling structure. Therefore, achieving a high energy density while maintaining the high power density of SCs has become a challenge.<sup>2</sup> TMOs with perovskite structures have been used as functional materials in energy-related fields, acting as electrodes.<sup>1</sup> For instance, ruthenates (SrRuO<sub>3</sub>),<sup>5</sup> titanates (SrTiO<sub>3</sub>),<sup>6</sup> aluminates (LaAlO<sub>3</sub>),<sup>7</sup> nickelates (CeNiO<sub>3</sub>), cobaltites (CeCoO<sub>3</sub>), and cuprates (CeCuO<sub>3</sub>),<sup>8</sup> have been used for these applications. These perovskites have emerged as alternatives for use as SCs in which high power and energy density are achieved, along with improved stability during cycling tests.

**Received:** May 7, 2025

**Revised:** June 17, 2025

**Accepted:** June 20, 2025

**Published:** July 14, 2025



Concerning perovskites, those based on strontium have gained attention for applications in SCs because of their abundance, ionic and electronic conductivity, and tolerance to the reduction–oxidation cycle.<sup>9</sup> In this sense, Tomar et al.<sup>6</sup> synthesized mesoporous SrTiO<sub>3</sub>-based materials by the sol–gel method and applied them in aqueous and solid-state SCs. The authors reported that the material exhibits a high specific capacitance (212.5 F g<sup>-1</sup> at 0.63 A g<sup>-1</sup>), good capacitance retention (74.5% at 2.5 A g<sup>-1</sup>), excellent cycling stability (99% after 5000 cycles), high energy density (27.8 W h kg<sup>-1</sup>), and power density (1921 W kg<sup>-1</sup>). George et al.<sup>10</sup> have investigated the effect of doping with Ba, Ca, Co, Fe, and Ni cations at the Sr-sites in strontium Manganite (SrMnO<sub>3</sub>), on the capacitive properties and showed superior capacitive properties for the doped SrMnO<sub>3</sub>, correlating it with the increased oxygen vacancies and structural distortions that favor charge transport and redox reactions. On the other hand, Lang et al.<sup>11</sup> prepared lanthanum Manganite-based perovskites doped with strontium (La<sub>1-x</sub>Sr<sub>x</sub>MnO<sub>3</sub>, LSM) for supercapacitor applications and showed that La<sub>0.85</sub>Sr<sub>0.15</sub>MnO<sub>3</sub> composition presented superior performance for applications as pseudocapacitance electrode materials. These authors associated this efficiency with the redox reaction of the anion intercalation corresponding to the surface redox processes of Mn<sup>2+</sup>/Mn<sup>3+</sup> and Mn<sup>3+</sup>/Mn<sup>4+</sup>.

Like A-site substitution, partial substitution at the B-site in the ABO<sub>3</sub>-type perovskites has been proven to be a feasible approach to modify the crystal and electronic structures to optimize the optical, and electrochemical properties and thus increase the capacitance in the materials.<sup>10–12</sup> Specifically, inducing distortions in the lattice and changing the oxidation states of the B-site cations may increase the concentration of oxygen vacancies. As a result, it may boost the capacitive performance of SC electrode materials. Thus, B-site substituted perovskites have also been investigated, such as cobaltites/niobates (SrCo<sub>0.875</sub>Nb<sub>0.125</sub>O<sub>3</sub>),<sup>13</sup> and ferrites/zirconates (SrFe<sub>1-x</sub>Zr<sub>x</sub>O<sub>3-δ</sub>).<sup>13</sup> It is possible to modify the structural symmetry of the perovskite through hetero ion doping to optimize its electronic properties and functionalities. In addition to these materials, tin-based perovskites or ilmenites, both with the formula ASnO<sub>3</sub> have also received attention due to their performances in electrochemical energy storage.<sup>1,12,14–19</sup> Concerning the tin-based perovskites, Veerappan et al.<sup>16</sup> prepared materials based on pristine BaSnO<sub>3</sub> and a composite of BaSnO<sub>3</sub>/20 wt % of reduced graphene oxide (rGO) and reported excellent specific capacity and cycling behavior of the perovskite BaSnO<sub>3</sub> nanoparticles decorated on two-dimensional graphene flakes. The BaSnO<sub>3</sub>/rGO20 composite showed a maximum capacity of 1200 mA h g<sup>-1</sup> at 0.5 C (650 mA g<sup>-1</sup>), which was far higher than that observed for single species, BaSnO<sub>3</sub> and rGO anodes. Recently, Elmushyakh and Alqahtani<sup>20</sup> prepared nanohybrids based on SrSnO<sub>3</sub>/rGO and showed a potential increase in capacitance and energy density due to the integration of rGO in the composite.

From this perspective, strontium stannate perovskite (SrSnO<sub>3</sub>) is a potential alternative material for applications in SCs. SrSnO<sub>3</sub> has shown interesting electronic properties, used for a variety of applications, including as a photocatalytic material,<sup>21</sup> electrode material for dye-sensitized solar cells,<sup>22</sup> alkali-ion battery,<sup>15</sup> drug sensing,<sup>23</sup> transistors,<sup>24</sup> and others. Although SrSnO<sub>3</sub> has been employed in its pure form or combined with other materials, doping may effectively enhance the charge transport in SrSnO<sub>3</sub>.

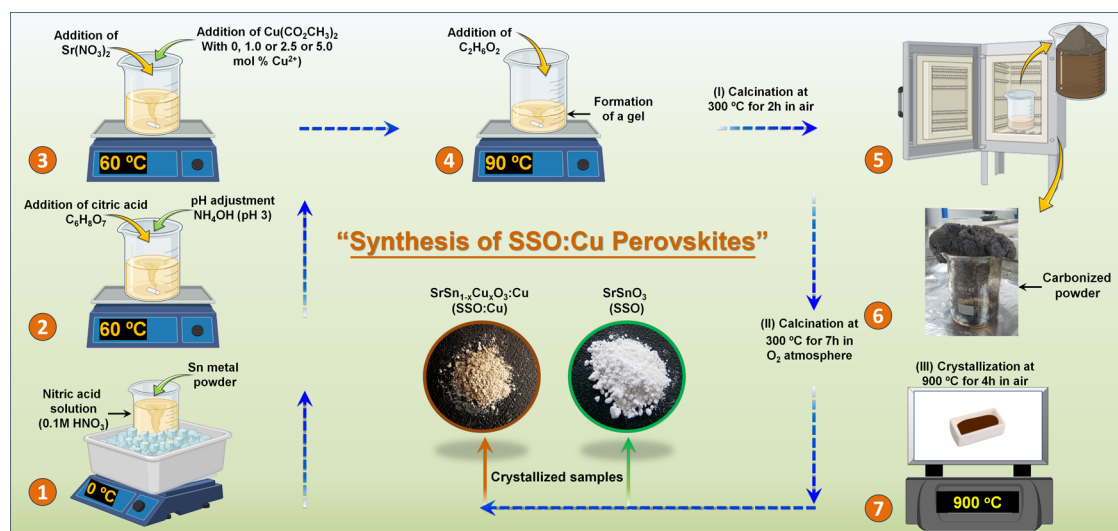
Regarding the doping process, the incorporation of Cu cations into the lattice of different materials, from simple oxides to inorganic and hybrid perovskite-based compounds, has attracted the interest of many researchers in different fields, especially in electrochemistry, and some studies, including theoretical ones, can be found in the literature.<sup>25–32</sup> Relatively few studies of Cu-doped perovskite materials, both inorganic and hybrid ones, can be found in the literature. For instance, Tezel et al.<sup>32</sup> investigated the effect of different dopants on the supercapacitive properties of thin films of hybrid halide MAPbX<sub>3</sub> perovskites deposited on fluorine tin oxide (FTO) substrates. These authors reported that Mn, Gd, Sn, Nb, and Cu are often preferred to dope perovskite materials due to their excellent dispersion and tendency to high electrical conductivity. Tezel et al.<sup>32</sup> showed that a significant energy storage capacity of MAPbX<sub>3</sub> perovskites was achieved with the optimal dopant concentration of 2 mol % Cu. About inorganic perovskites, Ramadan and Ramadan<sup>33</sup> fabricated asymmetric supercapacitors based on Bi<sub>1-x</sub>Cu<sub>x</sub>FeO<sub>3</sub> and found that 5 mol % Cu<sup>2+</sup> was the optimum doping concentration to improve the fast electrolyte ion diffusion, enhancing the capacitive properties of the material. The authors associated this capacitive efficiency with the increase of oxygen vacancies and Fe<sup>2+</sup>/Fe<sup>3+</sup> ratio induced by the Cu<sup>2+</sup>/Bi<sup>3+</sup> substitution.

Based on all these facts, this work aims to synthesize SrSnO<sub>3</sub> perovskites doped with different concentrations of copper (1, 2.5, and 5 mol % Cu<sup>2+</sup>) by a modified Pechini method for applications as SCs. Although some studies have focused on incorporating copper in other perovskites, a systematic investigation of SrSnO<sub>3</sub>-based materials for supercapacitor applications has not been reported yet. Furthermore, the impact of Cu(II)-doping on the perovskite crystal structure, optical and electronic properties, and their high-performance supercapacitance was thoroughly studied for the first time. Notably, the electrode materials based on Cu(II)-doped SrSnO<sub>3</sub> perovskites fabricated in the current work show a remarkably high specific capacitance, high energy, and power density, as well as outstanding cyclic stability, demonstrating their great potential use as high-performance energy-density supercapacitors.

## ■ MATERIALS AND METHODS

**Materials Preparation.** For the synthesis of the SrSn<sub>1-x</sub>Cu<sub>x</sub>O<sub>3</sub> ( $x = 0, 1, 2.5, \text{ and } 5 \text{ mol } \%$ ) perovskites, tin metal powder (Sn, Vetec 99.0%), strontium nitrate (Sr(NO<sub>3</sub>)<sub>2</sub>, Vetec 99.0%), copper(II) acetate monohydrate (Cu-(CO<sub>2</sub>CH<sub>3</sub>)<sub>2</sub>·H<sub>2</sub>O, Alfa Aesar 99.9%), citric acid monohydrate (C<sub>6</sub>H<sub>8</sub>O<sub>7</sub>·H<sub>2</sub>O, Cargill 99.5%), ammonium hydroxide (NH<sub>4</sub>OH, Vetec 99%), and ethylene glycol (C<sub>2</sub>H<sub>6</sub>O<sub>2</sub>, Vetec 99.5%) were used as starting materials without any further purification.

**Synthesis Procedure.** The SrSn<sub>1-x</sub>Cu<sub>x</sub>O<sub>3</sub> samples ( $x = 0, 1, 2.5, \text{ and } 5 \text{ mol } \%$  Cu doping) labeled as SSO, SSO:Cu1, SSO:Cu2.5, and SSO:Cu5, respectively, were synthesized by a modified Pechini method as described in our previous works for tin-based materials.<sup>34–36</sup> Initially, the Sn metal powder was dissolved in a 0.1 mol L<sup>-1</sup> nitric acid solution under constant stirring in an ice bath, maintaining the temperature at 0 °C.<sup>35,37</sup> The complete solubilization of tin metal to form oxidized Sn<sup>4+</sup> must occur, specifically, at 0 °C to prevent overheating, control reaction rates, and improve the yield of the desired Sn<sup>4+</sup>-citrate complex. Because this oxidation reaction is exothermic, temperature variations may favor side

Scheme 1. Schematic Diagram for the Synthesis Procedure of the  $\text{SrSn}_{1-x}\text{Cu}_x\text{O}_3$  (SSO:Cu $_x$ ) Samples

reactions, leading to the formation of undesirable intermediates. Therefore, after complete dissolution of the tin metal at  $0^\circ\text{C}$ , a stoichiometric amount of anhydrous citric acid (CA), in a ratio of 3:1 CA:cation was added to the solution, adjusting the pH to 3 by adding ammonium hydroxide. Next, stoichiometric amounts of strontium nitrate and copper(II) acetate monohydrate (for Cu-doped samples) were added to the tin citrate solution under constant stirring and heating at  $70^\circ\text{C}$ . Finally, ethylene glycol (EG) was added to the solution in a 40:60 mass ratio (EG:CA), increasing the temperature to  $90^\circ\text{C}$  to obtain the polymeric precursor solution. This solution was heat-treated at  $300^\circ\text{C}$  for 2 h to obtain the carbonized precursor powder. Secondary thermal treatments were performed at  $300^\circ\text{C}$  for 7 h in an  $\text{O}_2$  atmosphere to burn off the organic matter. This step minimizes the creation of ionic defects, such as oxygen vacancies and reduced species, facilitating the crystallization of the desired perovskite phase, with minimal formation of intermediates. Crystallization of  $\text{SrCO}_3$  occurs at a low temperature, whereas  $\text{SrSnO}_3$  in samples synthesized by a modified Pechini method begins at  $600^\circ\text{C}$ .<sup>38,39</sup> Thus, removing organic matter beforehand is crucial to obtaining the desired perovskite. After eliminating the organic matter from the precursor powders, the samples were calcined at  $900^\circ\text{C}$  for 4 h to obtain the desired well-crystallized material, without residual carbon traces. The synthesis procedure is summarized in Scheme 1.

**Materials Characterization.** Experimental X-ray powder diffraction (XRD) patterns were acquired in a Bragg–Brentano geometry in continuous mode with a scan speed of  $0.02^\circ\text{ s}^{-1}$  in a  $2\theta$  range from  $10^\circ$  to  $140^\circ$  using an Automated Multipurpose Powder X-ray Diffractometer XRDynamic 500 by Anton Paar equipped with a Primux 3000 sealed-tube Cu X-ray source and a Pixos 2000 solid-state hybrid pixel detector. For further structural investigations, room temperature Synchrotron X-ray powder diffraction (S-XRD) measurements were also performed using the powder diffractometer at the BL-10 beamline of the Australian Synchrotron.<sup>40</sup> During the S-XRD experiments, the samples were ground into a fine powder and housed in 0.2 mm glass capillaries that were rotated during measurements according to a Debye–Scherrer geometry. The beam energy was set to  $\sim 15\text{ keV}$  ( $\lambda = 0.82594(5)\text{ \AA}$ ) calibrated using a NIST 660b  $\text{LaB}_6$  a standard reference

material. The crystal structure of the samples was then determined by the Rietveld refinement method as implemented in the GSASII software package.<sup>41</sup> Near-edge X-ray absorption fine structure (XANES/NEXAFS) spectroscopy measurements on copper L-edge and oxygen K-edge were performed at the soft X-ray spectroscopy beamline of the Australian Synchrotron.<sup>42</sup> The samples were finely dusted onto conducting carbon tape placed on a gold disk, which was inserted into the vacuum chamber via a load lock. The samples were analyzed in ultrahigh vacuum (UHV) better than  $10^{-9}$  mbar, and the spectra were collected in a total electron yield (TEY) mode in the region of 900–995 eV for the Cu L-edge and 520–600 eV for the O K-edge with 0.1 eV per step. All the NEXAFS spectra were normalized using Athena software.<sup>43</sup> The infrared (FT-IR) spectra ( $400\text{--}4000\text{ cm}^{-1}$ ) were collected using a Shimadzu IRPrestige21 spectrophotometer using KBr pellets. Raman measurements were conducted using a Renishaw inVia Raman microscope. High-resolution Raman spectra were collected in dynamic mode using an  $\text{Ar}^+$  laser (514 nm wavelength) and a 2400 lines/mm grating, achieving a spectral resolution of approximately  $0.5\text{ cm}^{-1}$ . The spectra were scanned over a range of  $50\text{--}1000\text{ cm}^{-1}$ . UV–vis absorption spectroscopy analyses were performed in a Shimadzu UV-2550 spectrophotometer in diffuse reflectance mode with a spherical integration accessory. The samples were analyzed in wavelengths ranging from 190 to 900 nm. Pure barium sulfate ( $\text{BaSO}_4$ ) powder was used as a standard reference material for background measurement. Electron paramagnetic resonance spectroscopy (EPR) measurements were conducted on a Bruker E-500 ELEXSYS X-band (9.88 GHz) spectrometer at room temperature. The Zeta potential measurements were measured using a Zetasizer Nano Series with a (He–Ne) laser of 633 nm (Malvern Panalytical, U.K.). A  $0.05\text{ g L}^{-1}$  suspension of the different perovskites was prepared using a 0.1 M  $\text{NaNO}_3$  solution. Aliquots of 10 mL of the suspensions were sonicated at room temperature, and pH values were adjusted by adding 0.1 M  $\text{HNO}_3$  or 0.1 M  $\text{NaOH}$  solutions.

**Electrochemical Characterization and Fabrication of the Supercapacitor Device.** The electrochemical characterization of the material was performed with the aid of Biologic VMP 300 multipotentiostat using the double electrode system

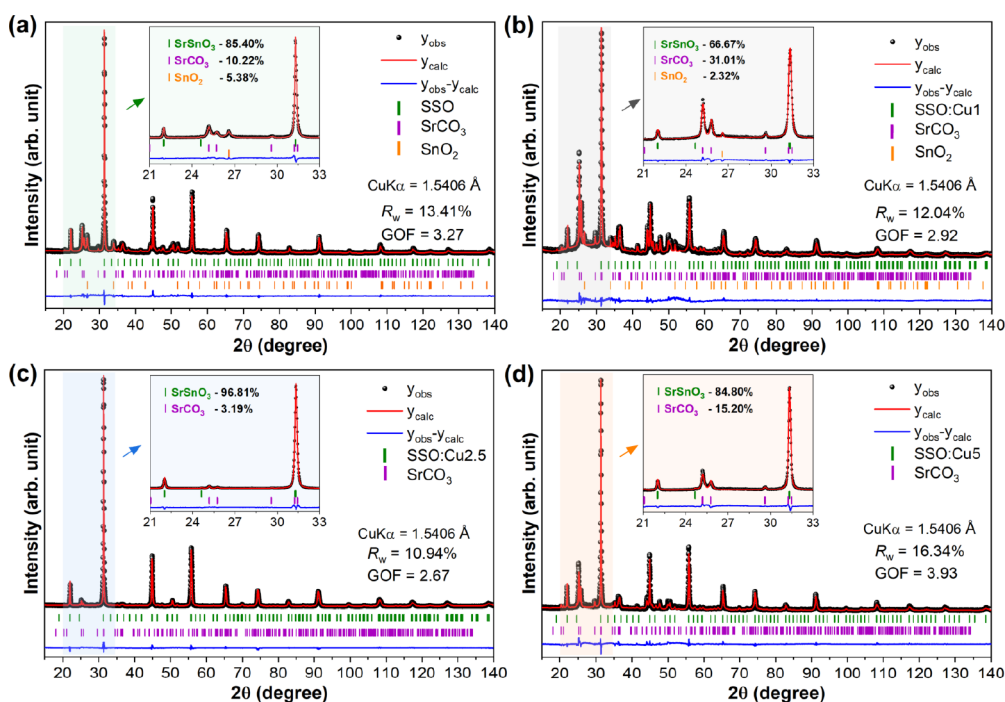


**Figure 1.** Rietveld profiles of the XRD patterns for SSO (a), SSO:Cu1 (b), SSO:Cu2.5 (c), and SSO:Cu5 (d) samples. The vertical markers indicate the positions of the space group allowed Bragg reflections for the main orthorhombic *Pbnm* perovskite phase,  $\text{SrCO}_3$ , and  $\text{SnO}_2$ . The insets depict a zoom into the region 21–33°. The fraction of the phases is indicated.

configuration, where the double electrode materials are symmetrically placed in powder form and separated by a glass fiber separator with  $\text{LiPF}_6$  electrolyte. Each electrode was assembled with 3 mg of active material (equivalent to a mass loading of approximately  $1.70 \text{ mg cm}^2$ ), uniformly deposited on stainless steel bolts (15 mm diameter) serving as current collectors. The material was characterized by cyclic voltammetry (CV), electrochemical impedance spectroscopy (EIS), and galvanostatic cycling with potential limitation (GCPL). CV measurements were carried out at a voltage range between 0 and 2.5 V at varying scan rates ranging from 1 to  $200 \text{ mV s}^{-1}$ . EIS tests were performed by applying a sinusoidal signal of 10 mV in a 10 to 1 MHz frequency range. GCPL tests were performed in a voltage window between  $-2$  and 2 V at a specific current of  $0.1 \text{ A g}^{-1}$ .

## RESULTS AND DISCUSSION

The long-range structural order of the SSO:Cu $x$  (with  $x = 0, 1, 2.5$ , and 5 mol %) samples was investigated by X-ray powder diffraction (XRD), as indicated in Figure 1. XRD patterns showed that the pristine and  $\text{Cu}^{2+}$ -doped SSO samples crystallized in an orthorhombic-type *Pbnm* structure, whose diffraction peaks were indexed according to the ICSD 90846 file.<sup>44</sup> No additional diffraction peaks related to any copper-based compounds were observed in the Cu(II)-doped SSO samples, indicating the incorporation of the  $\text{Cu}^{2+}$  cations into the crystal lattice.<sup>45</sup> To understand this better, structural refinements were performed using the Rietveld method as implemented in the GSAS II software. The Rietveld XRD profiles are shown in Figure 1a–d, and the refined parameters are listed in Tables 1 and S1.

The refinements confirmed that the samples adopt an orthorhombic *Pbnm* symmetry, presenting distinct lattice parameters, with the presence of  $\text{SrCO}_3$  and  $\text{SnO}_2$  as secondary phases (Table S1), especially in the pristine SSO

**Table 1. Refined Lattice Parameters for the SSO and SSC:Cu $x$  Samples**

	SSO	SSO:Cu1	SSO:Cu2.5	SSO:Cu5
space group	<i>Pbnm</i>	<i>Pbnm</i>	<i>Pbnm</i>	<i>Pbnm</i>
<i>a</i> (Å)	5.7081(5)	5.7143(10)	5.71621(19)	5.7094(26)
<i>b</i> (Å)	5.7071(7)	5.7014(16)	5.70494(28)	5.7050(16)
<i>c</i> (Å)	8.0773(5)	8.0668(28)	8.06130(31)	8.068(4)
<i>V</i> (Å <sup>3</sup> )	263.132(7)	262.812(14)	262.884(5)	262.791(9)
GOF	3.27	2.92	2.67	3.93
<i>R<sub>w</sub></i> (%)	13.41	12.04	10.94	16.34

and SSO:Cu1 samples. The samples containing a higher amount of  $\text{Cu}^{2+}$  did not present  $\text{SnO}_2$  as a secondary phase. The sample SSO:Cu2.5 had the lowest amount of secondary phase in the composition (only 2.32% of  $\text{SrCO}_3$ ).  $\text{SrCO}_3$  crystallizes at low temperature and its presence is commonly observed in strontium-based perovskites, particularly samples synthesized using Pechini-based methods, which involve the formation of metal-citrate complexes and a significant content of organic matter.<sup>38</sup> Without thermal treatment in an  $\text{O}_2$  atmosphere, higher concentrations of ionic defects such as oxygen vacancies and reduced cations, as well as increased  $\text{SrCO}_3$  formation, can occur. Excessive amounts of these can negatively impact the final target materials' application.<sup>37,39</sup>

Concerning the refined lattice parameters listed in Table S1, the pristine SSO sample showed the largest *b* and *c* parameters and the highest unit cell volume (*V*) compared to the other samples. Upon adding  $\text{Cu}^{2+}$ , slight variations in the lattice parameters were observed, with a decrease in the unit cell volume. In this context, it is essential to compare the ionic radii size of both the dopant cation ( $\text{Cu}^{2+} = 0.730 \text{ Å}$ , CN = 6) and the cation to be replaced ( $\text{Sn}^{4+} = 0.690 \text{ Å}$ , CN = 6) occupying the same coordination site. Incorporating a larger cation like  $\text{Cu}^{2+}$  at the  $\text{Sn}^{4+}$ -site of the  $\text{SrSnO}_3$  structure might lead to an

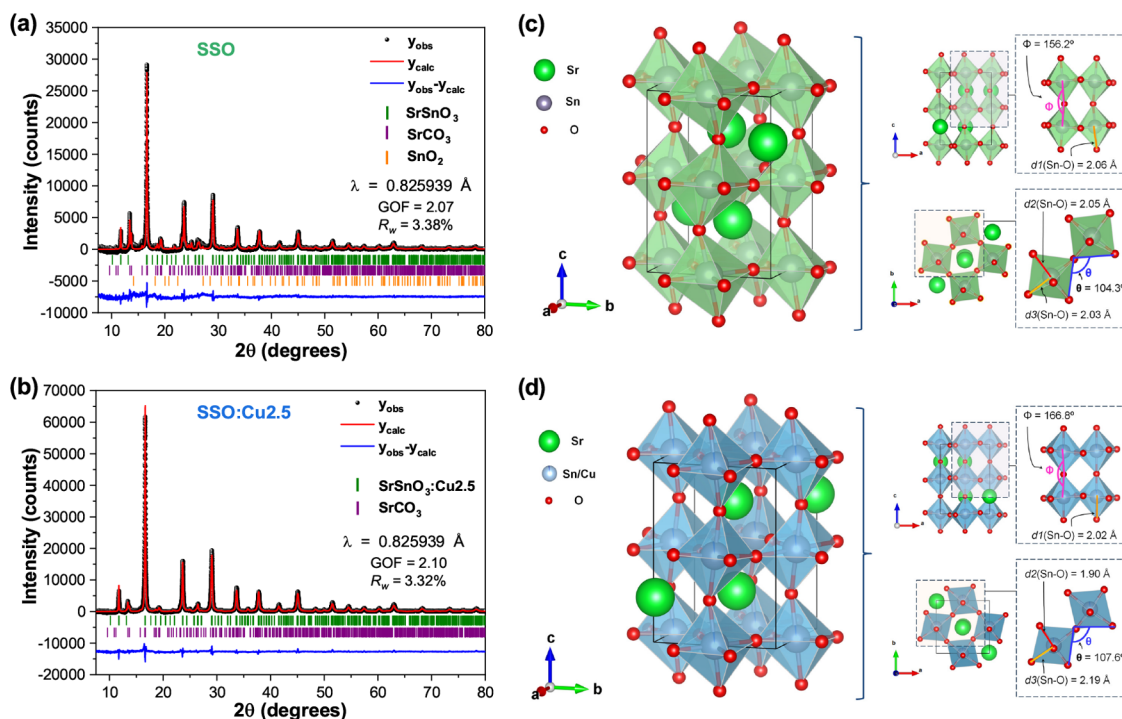


**Figure 2.** Rietveld profiles of the S-XRD patterns for SSO (a), and SSO:Cu<sub>2.5</sub> (b) samples. The vertical markers indicate the positions of the space group allowed Bragg reflections for the main orthorhombic *Pbnm* perovskite phase, SrCO<sub>3</sub>, and SnO<sub>2</sub>. Representation of the orthorhombic *Pbnm* Perovskite structure obtained for SSO (c) and SSO:Cu<sub>2.5</sub> (d) samples, and different projections showing *d*(Sn–O) bond distances and bond angles  $\theta$  and  $\phi$  related to in-plane and out-of-plane interoctahedra [SnO<sub>6</sub>] distortions, respectively.

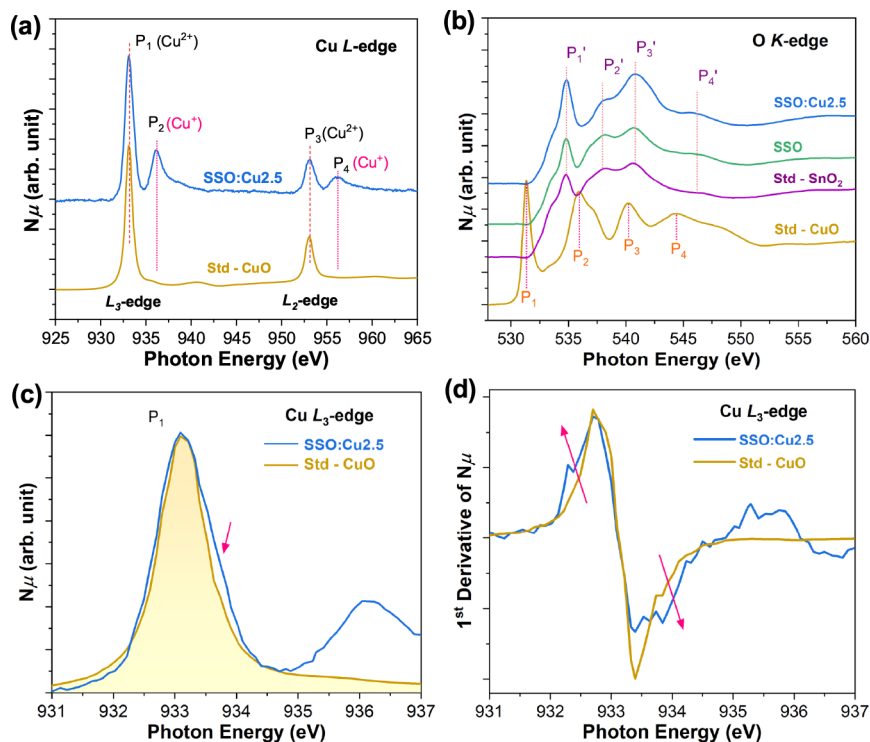


**Figure 3.** Normalized Cu L-edge (a), O K-edge (b) XANES/NEXAFS spectra of the SSO and SSO:Cu<sub>2.5</sub>, (c) normalized Cu L<sub>3</sub>-edge spectra, and (d) first derivative of the normalized Cu L<sub>3</sub>-edge absorption spectra. Std-SnO<sub>2</sub> and std-CuO correspond to bulk samples of SnO<sub>2</sub> and CuO, respectively. The pink arrows indicate variations in the Cu L<sub>3</sub>-edge spectra.

expansion of the unit cell volume. Surprisingly, such behavior was not observed in the present case, rather the incorporation of Cu<sup>2+</sup> did not result in a significant variation in the lattice parameters of SrSnO<sub>3</sub>. This behavior might be due to the

formation of different defects in the perovskite lattice, such as charged vacancies that lead to lattice contraction, which may compensate the unit cell expansion by Cu<sup>2+</sup> addition. According to Aidhy et al.,<sup>46</sup> charged vacancies are likely to

be more stable in oxide structures under compressive strain. However, the doping process induced a change in crystallinity and long-range structural order in the samples, as indicated by the full width at half-maximum (FWHM) values and the average crystallite size ( $D_C$ ) estimated by the Scherrer equation regarding the highest intense 112 diffraction peak (Table S1). Such a behavior is consistent with reported works dealing with doped SrSnO<sub>3</sub> materials.<sup>45,47</sup>

A significant increase in long-range disorder was evident from the increase in the FWHM for the SSO:Cu1 sample compared to the pristine SSO sample. In contrast, samples containing higher amounts of dopant (2.5 and 5.0 mol % Cu<sup>2+</sup>) presented a higher long-range order compared to the sample containing 1 mol % Cu<sup>2+</sup>. According to Melo et al.,<sup>45</sup> this behavior may be related to mass diffusion due to vacancy formation, correlated with the substitution of Sn<sup>4+</sup> with a lower valence cation Cu<sup>2+</sup> and due to the possible reduction of Cu<sup>2+</sup> to Cu<sup>+</sup> induced by the calcination process. Additionally, undesirable phases affect the structural ordering of the main phase of the stannate perovskite in the samples. This was confirmed through the Rietveld refinements against synchrotron X-ray diffraction (S-XRD) combined with X-ray absorption near edge structure/near-edge X-ray absorption fine structure (XANES/NEXAFS) spectroscopy performed for the pristine SSO and SSO:Cu2.5 (that presented the lowest content of impurities). These data are shown in Figures 2 and 3, respectively.

The refinements against S-XRD patterns for the SSO and SSO:Cu2.5 samples are shown in Figure 2a,b and listed in Tables S2 and S3. The results confirm the presence of the same phases seen in the conventional XRD patterns (Table S2). The S-XRD data were more sensitive to changes induced by the presence of the SrCO<sub>3</sub> secondary phase and the dopant. As also shown in conventional XRD, the refinements against the S-XRD showed that the main perovskite phase adopts an orthorhombic structure with the *Pbnm* space group. Still, a small decrease in the lattice parameters and the unit cell volume was observed after Cu doping. The refinements also indicated that the formation of SrCO<sub>3</sub> in the samples decreases the crystallinity as noted in the lower peak intensities, while doping with Cu 2.5 mol % does not (Figure 2a,b). This may be due to the lack of Sr<sup>2+</sup> available to react with Sn<sup>4+</sup> to form the desired perovskite phase that might lead to the formation of a disordered phase, which is further supported by the diffuse background observed around  $2\theta = 30^\circ$ .

The increased long-range order observed after the incorporation of copper might have resulted from the lowest amount of the secondary phase in the sample as well as the formation of point defects, such as oxygen vacancy ( $V_O$ ), in response to the charge compensation mechanism due to Cu<sup>2+</sup>/Sn<sup>4+</sup> substitutions. Additionally, further generation of oxygen vacancies may occur because of the spontaneous reduction of Cu(II) to Cu(I), or even oxidation to Cu(III), species in the Cu(II)-doped SSO samples, and this reflects in the octahedral distortions inside the crystal structure of SSO:Cu2.5 when compared to SSO (Figure 2c,d).

As can be noticed, the structural characteristics vary in both samples concerning the symmetry and magnitude of octahedral distortion, evident from the distortion index ( $D$ ), quadratic elongation ( $\langle\lambda\rangle$ ), bond angle variation ( $\sigma^2$ ), and the calculated effective coordination number (ECN), as listed in Table S3.

The distortion index ( $D$ ), quadratic elongation ( $\langle\lambda\rangle$ ), and intraoctahedral bond angles ( $\sigma^2$ ) are three key quantitative

metrics used in crystallography used to assess how much a coordination polyhedron, such as an octahedron, deviates from its ideal geometry in a crystal lattice. These values represent the overall size distortion rather than just individual polyhedral variations and are derived from crystallographic parameters obtained through Rietveld refinements. These parameters were originally described by Robinson et al.<sup>48</sup>

The distortion index ( $D$ ) quantifies variations in bond lengths (B–O) between the central atom and its coordinating atoms, making it a useful descriptor for detecting the Jahn–Teller effect, particularly in Cu-containing systems. In octahedral systems, an ideal or undistorted octahedral geometry is represented by  $D = 0$ . As  $D$  increases, the octahedral distortion becomes more pronounced. Quadratic elongation ( $\langle\lambda\rangle$ ) measures the extent to which octahedron bond lengths are stretched compared to an ideal regular one, indicating how far the central atom is shifted toward one of the faces. In symmetric geometry,  $\langle\lambda\rangle$  is equal to 1, whereas values greater than 1 indicate more elongated octahedral bonds. Additionally, intraoctahedral bond angles variation ( $\sigma^2$ ) reflects changes in the O–B–O angles relative to the ideal  $90^\circ$  within a BO<sub>6</sub> octahedron. A higher  $\sigma^2$  indicates a more distorted octahedron. This approach has been widely used to assess octahedral distortions in various compounds, particularly the Sn-based systems, such as SnO<sub>2</sub>,<sup>37</sup> SrSnO<sub>3</sub>,<sup>21</sup> and CaSnO<sub>3</sub>.<sup>49</sup>

As noted, these octahedral distortions result in significant changes in the Sn–O and Cu/Sn–O bond lengths as depicted in Figure 2c,d. As expected, these results confirm the increased distortion inside the [SnO<sub>6</sub>] when copper is incorporated into the octahedral sites of the SrSnO<sub>3</sub> crystal lattice. These sites occupied by Cu ions are likely to be tetragonally elongated, due to the Jahn–Teller effect, as suggested by the ECN = 5.158 obtained in the refinements (Table S3). All these structural modifications are caused by the distinct atomic coordinates ( $x$ ,  $y$ ,  $z$ ) for Sr, Sn, and O atoms and their displacement parameters observed for the SSO and SSO:Cu2.5 samples (Table S3) compared to the initial structural model reported for pristine SrSnO<sub>3</sub> perovskite.<sup>44</sup> These variations in atomic positions among the samples reflect differences in structural ordering.

Figure 3a,b show the Cu L-edge and O K-edge XANES/NEXAFS spectra, respectively, for the SSO and SSO:Cu2.5 samples, and for the bulk CuO and SnO<sub>2</sub> as reference materials. The Cu L-edge XANES/NEXAFS spectrum of the CuO standard shows two peaks, P<sub>1</sub> and P<sub>3</sub> in the L<sub>3</sub> and L<sub>2</sub>-edge regions, respectively, with a spin–orbit coupling of  $\Delta E = 20.1$  eV. Conversely, the Cu L-edge spectrum of the SSO:Cu2.5 sample also shows the presence of additional peaks, P<sub>2</sub> and P<sub>4</sub>, in L<sub>3</sub>- and L<sub>2</sub>-edges with a spin–orbit coupling of  $\Delta E = 19.9$  eV, indicative of the presence of Cu<sup>+</sup> (Figure 3a). The estimated  $\Delta E$  values are close to those reported in the literature for Cu<sub>2</sub>O and CuO, respectively.<sup>50</sup> We emphasize that the cation reduction is typically observed in samples obtained by the modified Pechini method, which generates a reducing atmosphere created during the calcination process.<sup>34,39</sup> Peak broadening was observed as highlighted in Cu L<sub>3</sub>-edge (Figure 3c) and in first derivative of the normalized spectra (Figure 3d) of the SSO:Cu2.5 sample and CuO standard, confirming different local environments around the Cu ions, and providing evidence for a more distorted Cu geometry in SSO:Cu2.5 compared to CuO.

Qualitatively, the presence of copper ions—Cu<sup>2+</sup> [Ar] 3d<sup>9</sup> and Cu<sup>+</sup> [Ar] 3d<sup>10</sup>—in samples can reflect the spectral features

of the O K-edge and the energy position of the peaks as shown in Figure 3b. The O K-edge spectrum of the CuO shows four major peaks labeled  $P_1$ ,  $P_2$ ,  $P_3$ , and  $P_4$ , consistent with the literature.<sup>50–52</sup> The peak  $P_1$ , at 531.3 eV, is assigned to  $1s \rightarrow 3e_g$  transition, where  $3e_g$  is formed from the hybridization of O 2p and Cu 3d orbitals. The other broad peaks ( $P_2$ ,  $P_3$ , and  $P_4$ ) are assigned to transitions to the hybridized O 2p and 3p orbitals with Cu 4s and 4p states. In the spectra of the  $\text{SnO}_2$  standard and SSO-based samples, these peaks are shifted to higher photon energies and are labeled as  $P_1'$ ,  $P_2'$ ,  $P_3'$ , and  $P_4'$ , due to different orbital hybridization. In the case of the  $\text{SnO}_2$ , these features correspond to O 2p states hybridized with sp bands of the Sn ion, while in SSO-based samples the O 2p states will also be hybridized with the narrow d bands of the alkaline earth metal ion.<sup>21</sup>

According to the literature,<sup>21,53,54</sup> the  $P_1'$  and  $P_3'$  features in the O K-edge spectra of Cu-based compounds reflect the transitions from the O 1s core state to the unoccupied O 2p states that are hybridized with the 5sp bands of the Sn ion (Figure 3b). The peak labeled as  $P_1'$  is centered at 534.77, 534.78, and 534.83 eV in the spectrum of the  $\text{SnO}_2$  standard, SSO, and SSO:Cu2.5 samples, respectively (Figure 3b), and the separation energy between  $P_1'$  and  $P_3'$  in these samples is 5.86, 5.87, and 5.98 eV. In the spectra, the  $P_1'$  feature is similar to that of the  $\text{SnO}_2$  standard rather than the CuO one. The increased intensity of this peak in the spectrum of SSO:Cu2.5 indicates that Cu ions enter into the  $\text{SnO}_6$  octahedral sites as  $[\text{Cu}/\text{SnO}_6]$ , as suggested also by the Cu L-edge XANES and Rietveld refinements. Apart from these spectral characteristics, an increase in the intensity of the  $P_3'$  feature in the spectrum of SSO:Cu2.5 is observed. These variations indicate changes in local structure between samples. Additionally, the increase of  $P_3'$  and the small variation in the hump marked by  $P_4'$  at 546.11 eV in the O K-edge spectrum of SSO:Cu2.5 may indicate strong hybridization of the O 2p states with Cu 3d orbitals. These features in the O K-edge XANES spectra and those in the Cu L-edge XANES spectra suggest that mixed  $\text{Cu}^{2+}/\text{Cu}^+$  cations are successfully incorporated into the  $\text{SrSnO}_3$  lattice. Furthermore, no diffraction peaks related to any copper-based compounds, such as  $\text{Cu}_2\text{O}$  or CuO, were observed in the S-XRD patterns. Given the high signal-to-noise ratio of the synchrotron X-ray diffraction data, and hence sensitivity to very small amounts of crystalline impurities, it is concluded that no copper-containing impurities are present in the samples.

To further investigate the local symmetry of the perovskite phase, FTIR and Raman spectroscopy were performed, as shown in Figures S1 and 4, respectively. FTIR spectra (Figure S1) demonstrate the appearance of active vibration modes characteristic of the  $\text{SrSnO}_3$  crystal structure, with the presence of vibration modes for  $\text{SrCO}_3$ , as expected.

Like FTIR spectroscopy, Raman provides information regarding the short-range order of the material. The literature reports the existence of 24 active vibrational modes in Raman for  $\text{SrSnO}_3$  with a  $Pbnm$  orthorhombic structure, which corresponds to  $\Gamma_{\text{Raman}} = 7A_g + 5B_{1g} + 7B_{2g} + 5B_{3g}$ , in which some cannot be identified due to the low polarizability of the atoms and/or due to their overlap.<sup>21,55</sup>

Five regions can be distinguished in the Raman spectra for  $\text{SrSnO}_3$  perovskites,<sup>21,24</sup> associated with the lattice modes Sr–Sn–O<sub>3</sub>, stretching modes of the O–Sn–O, scissor vibration modes of Sn–O–Sn, torsional modes of  $\text{SnO}_3$ , and stretching modes of Sn–O. Bands at higher frequencies above 600  $\text{cm}^{-1}$

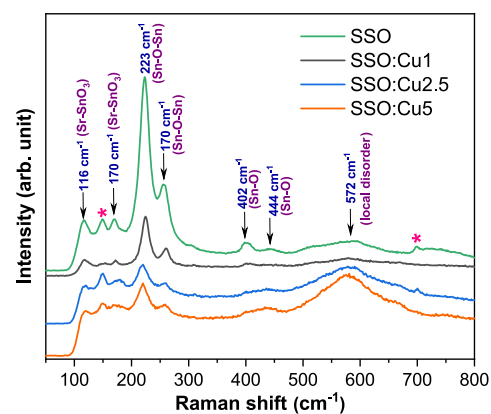
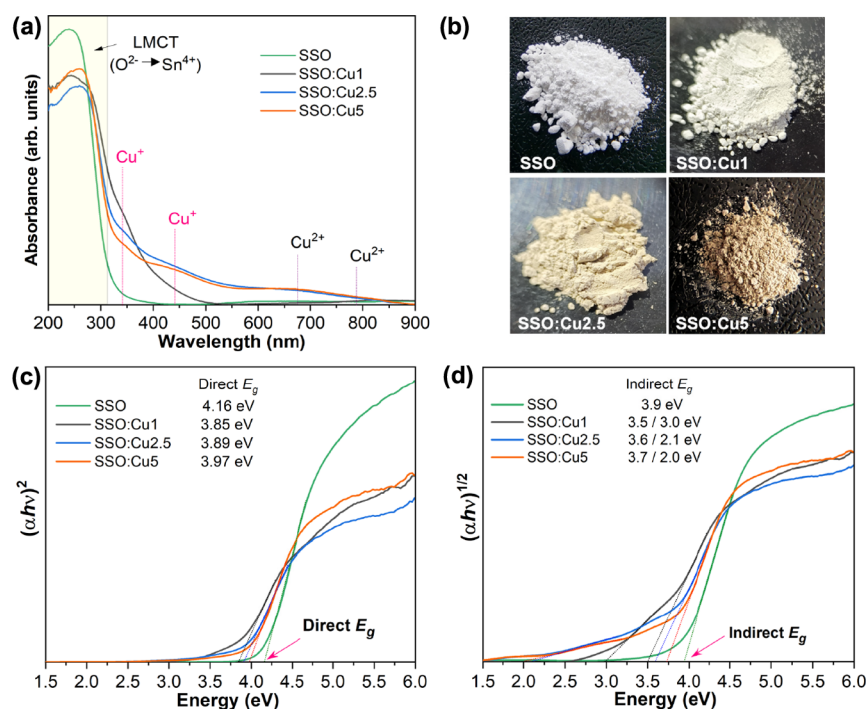


Figure 4. Raman spectra of the SSO and SSC:Cu<sub>x</sub> samples. Legend: \*  $\text{SrCO}_3$ .

may also be related to second-order scattering vibrations. Figure 4 shows the Raman spectra of the SSO and SSO:Cu samples. All the samples present similar spectra with a decrease in the peak intensity in the Cu-doped SSO samples. In the Raman spectrum of the pristine SSO sample, peaks at 116 and 170  $\text{cm}^{-1}$  were observed, associated with vibrational modes of Sr–SnO<sub>3</sub>. The intense peak at 223  $\text{cm}^{-1}$  and that at 257  $\text{cm}^{-1}$ , are assigned to the stretching modes of O–Sn–O and scissor modes of the Sn–O–Sn groups, respectively.<sup>21,24</sup> The peaks at 402 and 444  $\text{cm}^{-1}$  refer to the stretching modes of Sn–O bonds and torsional modes of the  $\text{SnO}_3^{2-}$  groups of the  $[\text{SnO}_6]$  octahedra.

For Cu-doped SSO materials, a broadening of most of the peaks, especially those related to the Sn–O, Sn–O–Sn, and O–Sn–O modes, indicates an increase of the short-range disorder when compared to the pristine SSO sample, suggesting  $\text{Cu}^{2+}/\text{Sn}^{4+}$  replacement in the perovskite lattice, which agrees with S-XRD and XANES spectroscopy. In particular, a pronounced broadening and slightly displacement to a lower frequency of the band at 223  $\text{cm}^{-1}$ , corresponding to the O–Sn–O stretching modes, might also indicate that the partial replacement of tin by copper promotes a considerable distortion of the  $\text{SnO}_6$  octahedra, agreeing with the bond angle variations, quadratic elongation, and distortion index parameters obtained by the Rietveld refinements against S-XRD for SSO and SSO:Cu2.5 samples. These distortions further generate a greater number of structural defects. The broadening of the peaks around 444  $\text{cm}^{-1}$  and especially the pronounced hump at 572  $\text{cm}^{-1}$  observed after Cu doping also indicates the formation of defects such as oxygen vacancies and increased short-range (local) structural disorder due to the higher contribution of the oxygen movements in the lattice,<sup>24</sup> also evidenced in the IR results. Other studies revealed the same spectral profile and suggest that it induces deformation in the host lattice.<sup>24,55</sup> Apart from the peaks assigned to the Raman modes of the main perovskite  $\text{SrSnO}_3$  phase, other peaks were observed at 147 and 701  $\text{cm}^{-1}$  (marked with \*) that were assigned to a secondary  $\text{SrCO}_3$  phase, also observed by IR, conventional XRD, and S-XRD results.

The absorption UV–vis spectra of the undoped and Cu-doped SSO samples shown in Figure 5a contain features due to ligand–metal charge-transfer (LMCT) and Cu d–d electronic transitions. The absorption band around 200 and 300 nm is assigned to the LMCT from  $\text{O}^{2-} \rightarrow \text{Sn}^{4+}$ . The low-intensity absorption bands, observed between 300 and 900 nm in the



**Figure 5.** UV-vis absorption spectra (a), color of the powder samples (b), and Tauc plots with the estimated direct (c) and indirect (d) band gap energy ( $E_g$ ) for the SSO and SSO:Cu systems.

Cu-doped SSO sample, that are absent in the spectrum of the undoped SSO sample, are attributed to d–d transitions of the Cu species.<sup>45</sup> The more Cu is added to the perovskite lattice, the more obvious and intense these absorption bands are. The absorption spectra of the samples were deconvoluted into different absorption Gaussian bands, as exemplified in Figure S2, and the spectral deconvolution data are listed in Table S4. The broad absorption bands and the deconvoluted Gaussian bands associated with the Cu ions confirm the formation of brownish-colored powder samples (Figure 5b).

A gradual increase in absorbance is observed with the appearance of absorption bands around 340 and 440 nm due to the  $3d^{10} \rightarrow 3d^9 4s^1$  electronic transitions of the  $Cu^+$  species. An increase in the absorption bands was also observed at around 650 and 780 nm, attributed to the  $Cu^{2+}$  electron transitions in tetragonally distorted octahedral symmetry,<sup>45</sup> agreeing with the Rietveld and XANES/NEXAFS results. The appearance of these bands related to mixed  $Cu^{2+}/Cu^+$  cations is in good agreement with XANES/NEXAFS spectroscopy, leading to increased short-range disorder in Cu-doped SSO systems. The observed variations in the absorption edge in the Cu-containing samples reveal the influence of the doping process on the electronic properties of the SSO perovskites. The increase in Cu doping can lead to different electronic transitions in the lattice, leading to a decrease in the band gap energies ( $E_g$ ) as shown in Figure 5c,d, which is consistent with the color change of the samples (Figure 5b).

The literature reports that  $SrSnO_3$  is an n-type semiconductor with an indirect band gap of approximately 4.0 eV.<sup>56,57</sup> Gao et al.<sup>58</sup> determined an indirect transition of 2.75 eV for  $SrSnO_3$  employing DFT calculations. However, recent works suggest that  $SrSnO_3$  also shows direct transitions. For instance, employing DFT calculations, Chantelle et al.<sup>21</sup> determined the band structure for  $SrSnO_3$ , presenting a direct allowed transition ( $\Gamma \rightarrow \Gamma$ ) of 4.03 eV. Thus, direct and

indirect transitions were considered to estimate the  $E_g$  values of the pristine and Cu-doped SSO samples. The estimated direct and indirect  $E_g$  transitions for the materials are presented in Figure 5c,d, respectively.<sup>59</sup>

Considering the direct  $E_g$ , the experimental value estimated for the pristine SSO sample was 4.1 eV, decreasing to 3.8 and 4.0 eV after Cu doping. The direct  $E_g$  values found for the samples synthesized in this study are close to those reported in the literature. Specifically, Chantelle et al.<sup>39</sup> and Honorio et al.<sup>60</sup> observed an experimental  $E_g$  value between 4.0–4.05 eV for  $SrSnO_3$  samples synthesized by the modified Pechini method. On the other hand, Zheng et al.<sup>61</sup> reported a direct  $E_g = 4.1$  eV for  $SrSnO_3$  samples obtained by the microwave-assisted hydrothermal method, while Lee et al.<sup>62</sup> reported a band gap of 4.01 eV for samples prepared by the conventional solid-state reaction. Other authors have reported lower  $E_g$  values of about 3.9 eV.<sup>63–65</sup>

The estimated indirect  $E_g$  value for SSO was 3.9 eV, which agrees with the experimental data reported in the literature.<sup>24</sup> For the Cu-doped SSO systems, it is expected that doping will reduce the band gap, whether the cationic substitution at the Sr and/or Sn sites in the  $SrSnO_3$  lattice, since they alter the symmetry of the oxide and induce the formation of defects in the lattice. The experimental values of the indirect  $E_g$  estimated for the Cu-doped SSO systems suggest that the indirect band gap is more affected by doping than the direct band gap. Specifically, doped samples showed only a 10% reduction in direct  $E_g$  values compared to pristine SSO. In contrast, the indirect  $E_g$  value estimated for SSO:Cu5 is nearly half of that observed for pristine SSO. Additionally, the indirect band gap exhibits sensitivity to the Cu content, decreasing continuously as more Cu is incorporated into the SSO lattice. This trend can be attributed to the introduction of midgap states originating from the Cu 3d orbitals ( $Cu [Ar] 4s^2 3d^9$ ).<sup>49</sup> These findings are consistent with those reported by Maul et al.,<sup>49</sup> who

employed DFT simulations to examine the effects of oxygen vacancies and Cu doping on the local structure and electronic band structure of  $\text{CaSnO}_3$ . Their study demonstrated that vacancy formation reduces the Sn atomic charge in undoped  $\text{CaSnO}_3$ . Furthermore, the electronic band structure and density-of-states (DOS) are modified depending on the specific Cu configurations in the  $\text{CaSnO}_3$  lattice, either with or without accompanying oxygen vacancies. Cu doping without oxygen vacancies introduces copper-derived states at the top of the valence band (VB), leading to a reduced band gap. Conversely, Cu doping with oxygen vacancies creates additional DOS at the top of the VB due to O p–Cu  $d_{z^2}/d_{xy}$  hybridization, and near the bottom of the conduction band (CB) from Cu  $d_{xy}$ –Sn p hybridization, resulting in a more significant band gap reduction, as observed in the current study. The decrease in the band gap through doping is further supported by the changes in the samples' color.

The presence of point defects, associated with paramagnetic species, was investigated by solid-state X-band continuous wave EPR spectroscopy, as displayed in Figure 6. In the EPR

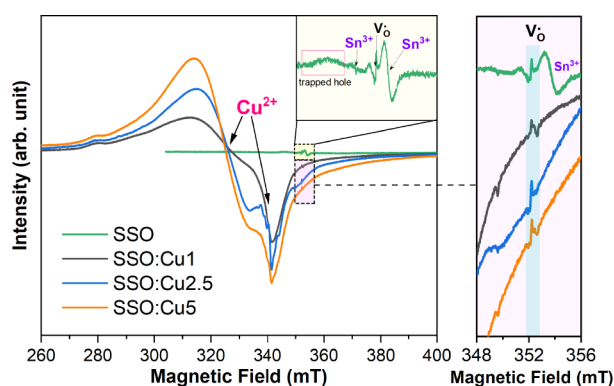


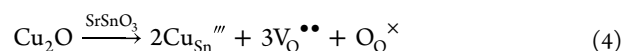
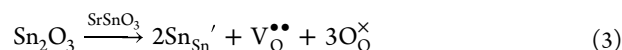
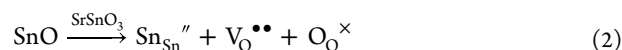
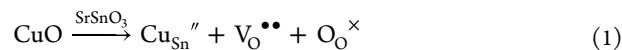
**Figure 6.** X-band EPR spectra of the SSO and SSO:Cu samples. The inset shows a zoom-in on the defect centers' EPR signal for the SSO sample.

spectrum of the pristine SSO sample, three resonance signals were observed at  $g = 2.0053$ ,  $2.001$ , and  $1.993$ , with a pronounced hump at a lower magnetic field, attributed to the valence band trapped hole of  $\text{O}^-$  centers. According to our previous EPR studies of  $\text{SrSnO}_3$ , the two resonances at  $g = 2.0053$  and  $1.993$  are related to  $\text{Sn}^{3+}$  centers. In contrast, the EPR signal with  $g = 2.001$  is attributed to single ionized oxygen vacancies ( $\text{V}_\text{O}^\bullet$ ).<sup>34</sup> In the Cu-doped SSO samples, the intensity of these signals seems to decrease, especially those associated with  $\text{Sn}^{3+}$  centers (Figure 6). This behavior may be due to the appearance of a strong resonant EPR signal with an additional splitting that is associated with the dopant. The intensity of the signal and peak-to-peak line width increase as a function of the Cu concentration in the samples, confirming the presence of  $\text{Cu}^{2+}$  cations in the samples. Associated with Rietveld refinements that did not show diffraction peaks and Raman spectroscopy that did not present optical modes related to any copper-based compounds, it can be concluded that the  $\text{Cu}^{2+}$  cations are successfully incorporated into the  $\text{SrSnO}_3$  lattice, even when higher doping amounts are used.

The appearance of the broad resonant signal is attributed to dipolar spin–spin interactions between the  $\text{Cu}^{2+}$  centers. According to the literature, the appearance of the additional splitting in the EPR resonance observed for Cu-containing

systems is characteristic of inhomogeneous crystal structures surrounding the  $\text{Cu}^{2+}$  centers.<sup>66–68</sup> An axial  $g$ -factor was estimated for the  $\text{Cu}^{2+}$  centers having  $g_\perp = 2.07$  and  $g_\parallel = 2.17$ , suggesting that the  $\text{Cu}^{2+}$  ions substitute the  $\text{Sn}^{4+}$  ions at the octahedral sites of the  $\text{SrSnO}_3$  crystal structure, as suggested by the refinements against the S-XRD pattern and XANES/NEXAFS spectroscopy. The variation in the peak-to-peak line width and the  $g$ -values in the EPR with the increase of the  $\text{Cu}^{2+}$ -content might be attributed to different dipolar exchange interactions existing between the  $\text{Cu}^{2+}$  ions at two distinct coordination environments, like an axially elongated octahedral geometry or pseudo rhombic distorted octahedral geometry in the perovskite lattice due to the Jahn–Teller (JT) instability of the  $3d^9$   $\text{Cu}^{2+}$  cations. These results are consistent with the structural characteristics proposed by the Rietveld refinements and the local structure around Cu ions, as indicated by XANES/NEXAFS.

The  $\text{Cu}^{2+}/\text{Sn}^{4+}$  substitution in the lattice induces the formation of  $\text{V}_\text{O}$  in response to a charge compensation mechanism in the system as represented in eq 1, written following Kröger–Vink's notation. The formation  $\text{V}_\text{O}$  in the systems may also be induced by reduction of  $\text{Sn}^{4+}$  to  $\text{Sn}^{2+}$  species (as previously reported for similar materials<sup>39,60</sup>) or even to a transient  $\text{Sn}^{3+}$  centers in the lattice as indicated by EPR data, as represented in eqs 2 and 3, respectively. The  $\text{Cu}^{2+}/\text{Sn}^{4+}$  substitution may also be accompanied by the reduction of both  $\text{Cu}^{2+}$  and  $\text{Sn}^{4+}$  to  $\text{Cu}^+$  and  $\text{Sn}^{3+}$ , respectively, in response to a charge compensation mechanism in the systems. This understanding is consistent with XANES/NEXAFS and UV–vis spectroscopy. In addition, the formation of reduced  $\text{Cu}^+$  would also lead to the formation of  $\text{V}_\text{O}$ , as illustrated in eq 4.



Apart from these defects, the formation of  $\text{SrCO}_3$  as a secondary phase in the samples suggests the creation of strontium vacancies ( $\text{V}_{\text{Sr}}''$ ) as displayed in eq 5:



Considering these possible point defects in Cu-doped SSO systems, the reduction of  $\text{Cu}^{2+}$  to  $\text{Cu}^+$  cations would lead to the formation of  $\text{V}_\text{O}$  (eq 4), being accompanied by significant oxidation of reduced  $\text{Sn}^{2+}$  to  $\text{Sn}^{3+}$  or further oxidation to  $\text{Sn}^{4+}$  or even preventing the reduced Sn species from being formed, achieving neutrality in the systems, or cation rearrangements into the lattice. This seems to be true since the EPR signal associated with the paramagnetic  $\text{Sn}^{3+}$  centers tends to diminish, while the  $\text{V}_\text{O}^\bullet$  signal is still evident even after doping. This spectral variation is highlighted by the selected region of the EPR spectra shown in Figure 6.

It is essential to note that the presence of all these point defects in the SSO:Cu systems can enhance the electronic conductivity of the materials and, consequently, their supercapacitive performance.<sup>69–72</sup>

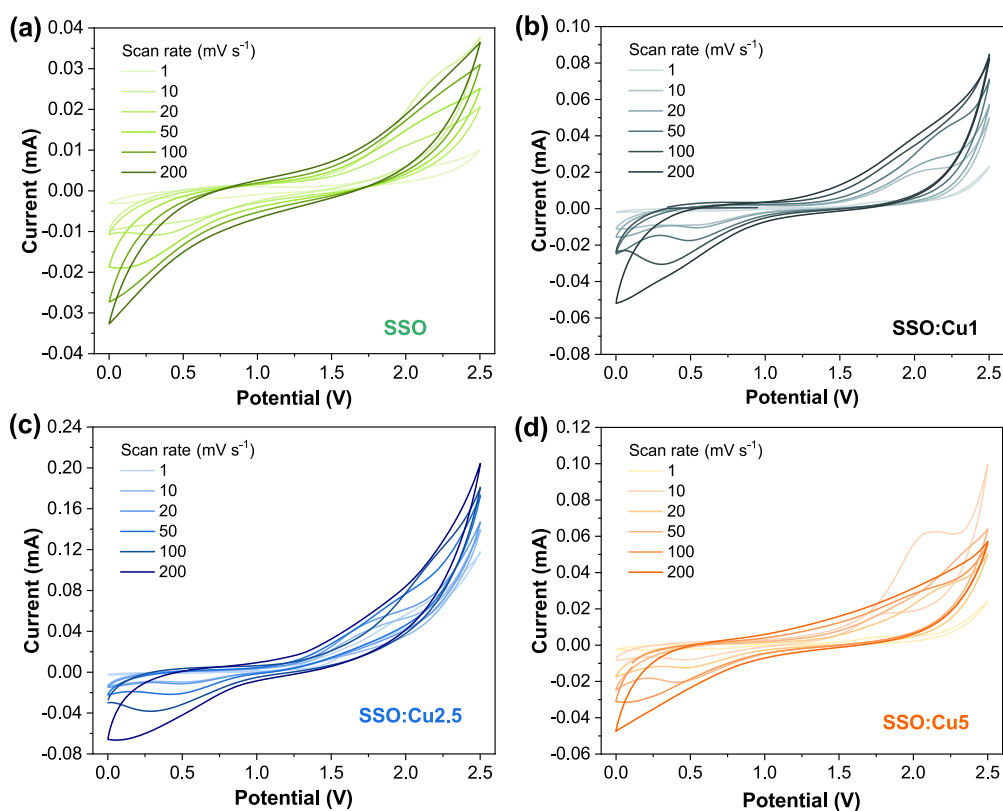


**Figure 7.** CV curves of the SSO (a), SSO:Cu1 (b), SSO:Cu2.5 (c), and SSO:Cu5 (d) used as electrode materials for supercapacitors measured at different scan rates.

The capacitive performance of undoped and Cu-doped SSO materials was studied using cyclic voltammetry (CV), galvanostatic charging/discharging (GCD), and impedance spectroscopy (EIS) measurements to investigate the potential application of these materials in supercapacitors (SCs). Cyclic voltammetry (CV) curves were recorded for the pristine SSO (Figure 7a) and SSO:Cu (Figure 7b–d) samples over the potential window from 0 to 2.5 V at scan rates varying from 1 to 200  $\text{mV s}^{-1}$ .

All the samples exhibited the same CV curve shape, featuring a pair of redox peaks that represent pseudocapacitive behavior, particularly for the SSO:Cu samples (Figure 7). At higher scan rates, the CV curves increase, indicating good charge diffusion at the electrode surface, high reversibility capacity, and excellent high-rate performance. The specific capacitance ( $C_s$ ) of all the electrodes was then calculated using eq 6

$$C_s = \frac{A}{2mk\Delta V} \quad (6)$$

where  $A$  is the area under the CV curve,  $m$  is the mass of the electrode material,  $k$  is the scan rate, and  $\Delta V$  is the voltage window.

The  $C_s$  for the SSO:Cu2.5 sample of  $613 \text{ F g}^{-1}$  at a scan rate of  $1 \text{ mV s}^{-1}$  was much higher than that observed for the other samples, as displayed in Figure 8. As the scan rate increases, the  $C_s$  of samples decreases due to the competing electrochemical reactions. The higher performance of SSO:Cu2.5 samples might be attributed to several factors. First, the induced defects in the perovskite structure associated with reduced  $\text{Cu}^+$  and  $\text{Sn}^{3+}$  cations, in addition to oxygen vacancies, as shown by XANES/NEXAFS, UV–vis, and EPR, play a crucial role in increasing the redox reactions and the

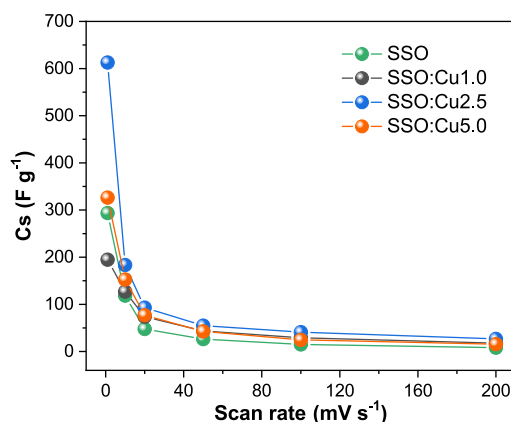


**Figure 8.** Variation of the specific capacitance in SSO, SSO:Cu1, SSO:Cu2.5, and SSO:Cu5 electrode materials at different scan rates.

electrochemical performance of the material. Furthermore, the surface charge Zeta potential (Figure S3) can also contribute differently to the active redox sites in the materials, resulting in different electrochemical behavior. In Cu-doped SSO materials, mixed valence  $\text{Cu}^{2+}/\text{Cu}^+$  plays the main role, but the presence of  $\text{SrCO}_3$  secondary phase is undesirable for the process. The reduced amount of the undesired  $\text{SrCO}_3$  phase in the SSO:Cu2.5 sample might lead to lower particle aggregation with the primary perovskite  $\text{SrSnO}_3$ :Cu phase, enhance ion diffusion, and improve electrochemical performance in the material. Furthermore, doping the perovskite with Cu altered the structure to balance the blockage, caused by  $\text{SrCO}_3$ , while increasing the conductivity, resulting in superior performance compared to the samples with 5 and 1% Cu

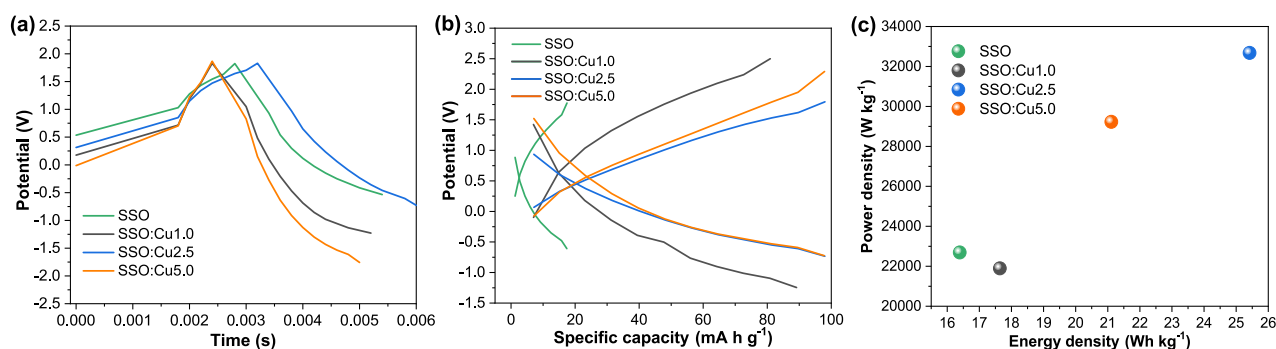


**Figure 9.** Time vs voltage (a), specific capacity vs voltage (b), and Ragone's plot (c) for the SC devices employing SSO, SSO:Cu1, SSO:Cu2.5, and SSO:Cu5 as electrode materials.

doping. SrSnO<sub>3</sub> (SSO) is not inherently recognized for its high electrochemical performance. However, integrating it with carbon-based materials can yield promising results in enhancing its specific capacity.<sup>20</sup> In the present case, doping modifications to SrSnO<sub>3</sub> demonstrated the greatest potential for significantly enhancing the material's specific capacity.

The GCPL measurements (Figure 9a) for the undoped and Cu-doped SSO samples showed a quasi-triangular shape, indicating the substantial influence of pseudocapacity, as expected, involving rapid Faradaic redox reactions, commonly associated with electrode materials based on metal oxides. The supercapacitor device employing SSO:Cu2.5 as electrode material exhibited a remarkably superior specific energy density ( $E_D$ ) and specific power density ( $P_D$ ) of 25.42 Wh kg<sup>-1</sup> g and 32.757 kW kg<sup>-1</sup>, respectively (Figure 9c) compared to the other prepared materials. Moreover, SSO:Cu2.5 and SSO:Cu5 both displayed the highest value of specific capacity of 100 mA h g<sup>-1</sup> (Figure 9b), which emphasizes the effect of the Cu dopant in the structure of SSO. Dunn's method was applied to the SSO:Cu2.5-based SC device to gain more insight into the working mechanism of the supercapacitor devices.

The Dunn method is widely used to distinguish between the capacitive and diffusive behavior of SCs.<sup>73–76</sup> Capacitive behavior indicates the dominance of the physical transport of ions, while diffusive behavior indicates the presence of Faradaic redox reactions.<sup>76,77</sup> The Dunn equation (eq 6) can be expressed as

$$I(V) = k_1 \cdot v + k_2 \sqrt{v} \quad (7)$$

where  $k_1$  and  $k_2$  represent the capacitive and diffusive currents, respectively, while  $v$  represents the scan rate. The relative contributions to the mechanism can be obtained by analyzing the slope and  $y$ -intercept of this formula.

The results from the Dunn method, displayed in Figure 10a,b, reveal the dominance of the diffusive mechanism with a contribution of around 63%. These results agree with those observed in the CV and GCPL measurements. The dominance of the diffusive mechanism is attributed to the pseudocapacitive behavior induced by the Cu dopant in the SSO structure. It is worth noting that the working mechanism of the SC devices is heavily influenced by the type and concentration of dopant in the SSO structure. It was reported that La and Nb dopants in SSO increase the capacitive mechanism of the SC devices through an increase in the number of active sites on the surface of the structure forming because of La<sup>3+</sup> and Nb<sup>5+</sup> replace Sn<sup>4+</sup> or Sr<sup>2+</sup>.<sup>1,78</sup> Conversely, Cu<sup>2+</sup> is known to promote diffusive behavior due to its strong redox nature, which increases the faradaic reactions in the bulk of the material.<sup>79</sup> It

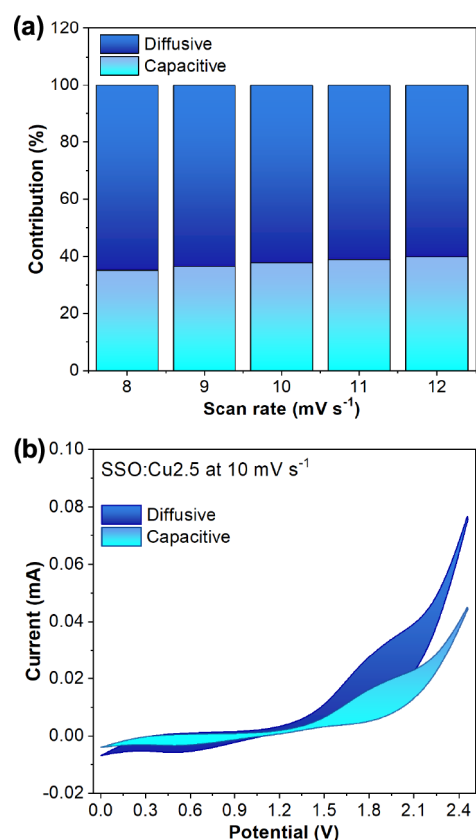


**Figure 10.** Dunn method analysis of capacitance contribution for SSO:Cu2.5: the histogram depicts the contribution ratio of capacitive effect and diffusion-controlled processes at various scans (a), and charge contribution of the capacitive effect and diffusion-controlled process at 10 mV s<sup>-1</sup> (b).

is important to note that a lower amount of SrCO<sub>3</sub> and the presence of mixed valence, especially Cu<sup>2+</sup>/Cu<sup>+</sup> states, introduces oxygen vacancies and structural distortions as observed for SSO:Cu2.5. These might be the main factors for its superior electrochemical performance. Furthermore, the secondary phase SrCO<sub>3</sub> in the sample is undesirable, showing a deleterious effect on the electrochemical processes in the samples, impacting the charge transport in and between the electrodes in the EDLC layer.

EIS was conducted to obtain information on the electrochemical properties of the synthesized perovskites. The analysis was performed at different potentials, and the equivalent circuit adjustment was constructed based on the

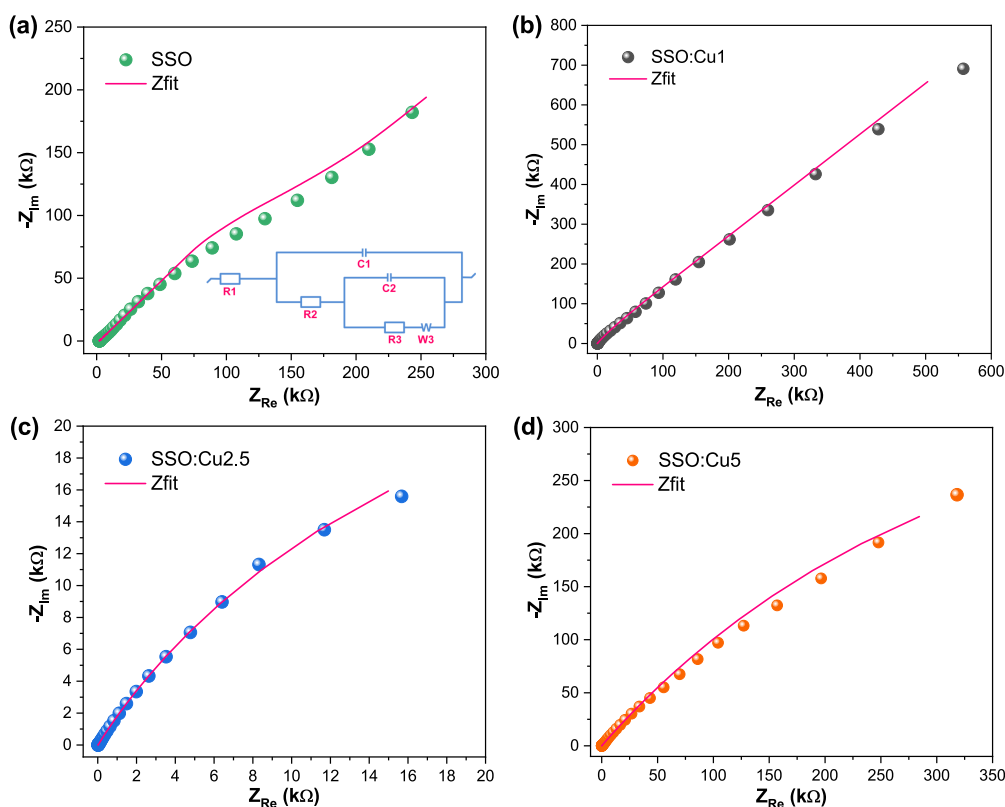


**Figure 11.** Nyquist plots for the SCs with electrodes of SSO (a), SSO:Cu1 (b), SSO:Cu2.5 (c), and SSO:Cu5 (d) materials, and Z-fit results based on the equivalent circuit model shown in the inset.

Nyquist plots for all four samples, as shown in Figure 11. The designed circuit consists of  $R_1$ , which represents the equivalent series resistance (ESR or  $R_s$ ) that shows the resistance between the electrode and the electrolyte,  $C_1$  represents the charge storage due to EDLC and pseudocapacitance,  $R_2$  is the charge transfer resistance,  $C_2$  is the pseudocapacitance,  $W_3$  is the Warburg element that represents the ion diffusion, and  $R_3$  is leakage resistance.

Table 2 summarizes the equivalent circuit fit results. A major decrease in the equivalent series resistance (ESR measured by

**Table 2.** Z-Fit Parameters Obtained after Fitting the Potentiostatic Electrochemical Impedance Spectroscopy (PEIS) Curves with the Equivalent Circuit Presented in the Inset of Figure 11a

	SSO	SSO:Cu1	SSO:Cu2.5	SSO:Cu5
$R_1$ ( $\Omega$ )	614	46.5	16.4	40.5
$C_1$ ( $\mu\text{F}$ )	20.7	48.6	590	190.5
$R_2$ ( $\Omega$ )	1.4	61.7	23.8	3.3
$C_2$ ( $\mu\text{F}$ )	0.32	5.16	28.9	10.3
$R_3$ ( $\Omega$ )	0.8	431.9	73.8	1.2

$R_1$ ) was observed postdoping Cu into the SSO structure. ESR includes the material's and electrolyte's ionic, intrinsic, and contact resistance. The decrease in ESR shows the effect of the dopant on the overall performance of SSO. Additionally, a significant increase in capacitance at the interface is observed from the rise of the  $C_1$  parameter in the results.

Upon comparing the electrochemical properties of the designed supercapacitors, the improved performance observed for the Cu-doped SSO materials is primarily attributed to the

doping process, which results in a material that consists predominantly of the perovskite  $\text{SrSnO}_3$ , with minimal formation of undesired phases. This behavior can be analyzed by examining the concentration of the perovskite and  $\text{SrCO}_3$  phases present in the materials estimated by Rietveld refinement. The contribution of these phases to specific capacitance ( $C_s$ ), energy density ( $E_D$ ), and power density ( $P_D$ ) in the materials can be understood as shown in Figure 12.

Figure 12a–c shows that an increase in the concentration of the primary perovskite  $\text{SrSnO}_3$  phase corresponds to higher  $C_s$ ,  $E_D$ , and  $P_D$  values. Interestingly, the SSO:Cu2.5 material, which contains an intermediate dopant concentration, exhibits the best electrochemical performance. This superior behavior is largely due to its composition, which consists almost entirely of the main perovskite phase ( $\sim 96.81\%$ ).

Conversely, despite SSO:Cu5.0 having the highest dopant concentration, it contains a greater proportion of the  $\text{SrCO}_3$  ( $\sim 15.22\%$ ) compared to SSO:Cu2.5. This indicates that a higher concentration of the main perovskite phase enhances the doping efficiency and improves the electrochemical performance in Cu-doped materials. In contrast, the increased presence of the  $\text{SrCO}_3$  secondary phase adversely affects performance (Figure 12d–f). Evidently,  $\text{SrCO}_3$  has a detrimental impact on the electrochemical properties in the supercapacitors.

To further investigate the potential application of SSO:Cu2.5 in operando, we succeeded in constructing a device composed of this material connected with a red light-emitting diode (LED), as shown in Figure 13 and the Supporting Video. The LED maintained a bright light for over 90 s, which reflects the material's voltage-holding capability. All samples could hold a 1.5 V potential, while SSO:Cu2.5

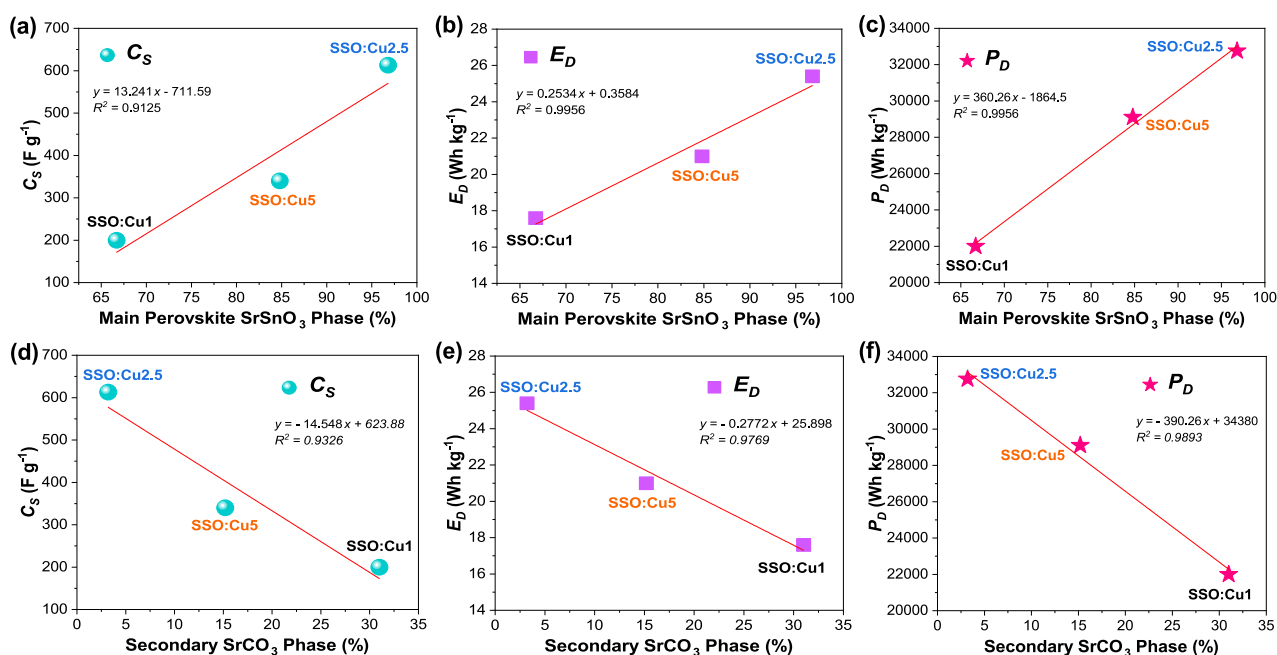


**Figure 12.** Contribution of the phases SrSnO<sub>3</sub> perovskite and SrCO<sub>3</sub> on the performance of the Cu-doped SSO samples as supercapacitors, considering the (a, d)  $C_s$ -specific capacitance, (b, e)  $E_D$ -energy density, and (c, f)  $P_D$ -power density.

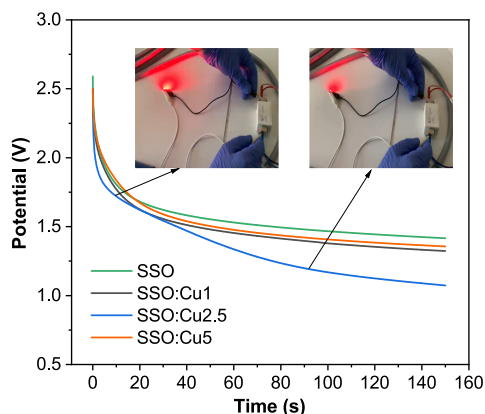


**Figure 13.** Voltage holding experiments using the undoped and Cu-doped SSO samples. The inset demonstrates the applicability of the supercapacitor devices, where an LED was powered for more than one min.

maintained a 1 V potential for the test period (150 s), higher than the required potential to light up the LED (0.8 V). The lower potential value of SSO:Cu2.5 is due to its lower resistance compared to the other studied samples.

The material generally provides a reliable and balanced performance in terms of specific capacitance, power, and energy density. Table 3 compares the performance of the proposed Cu-doped SSO with other systems based on perovskite-type oxides (SrSnO<sub>3</sub>/rGO, BiFeO<sub>3</sub>:Cu, SrRuO<sub>3</sub>/rGO, SrTiO<sub>3</sub>, SrMnO<sub>3</sub>:Ba, and La<sub>x</sub>Sr<sub>1-x</sub>CoO<sub>3</sub>) as well as other tin-based materials with an ilmenite-type structure such as MnSnO<sub>3</sub>, MnSnO<sub>3</sub>/rGO, FeSnO<sub>3</sub>, and NiSnO<sub>3</sub>.<sup>17,19,83,84</sup>

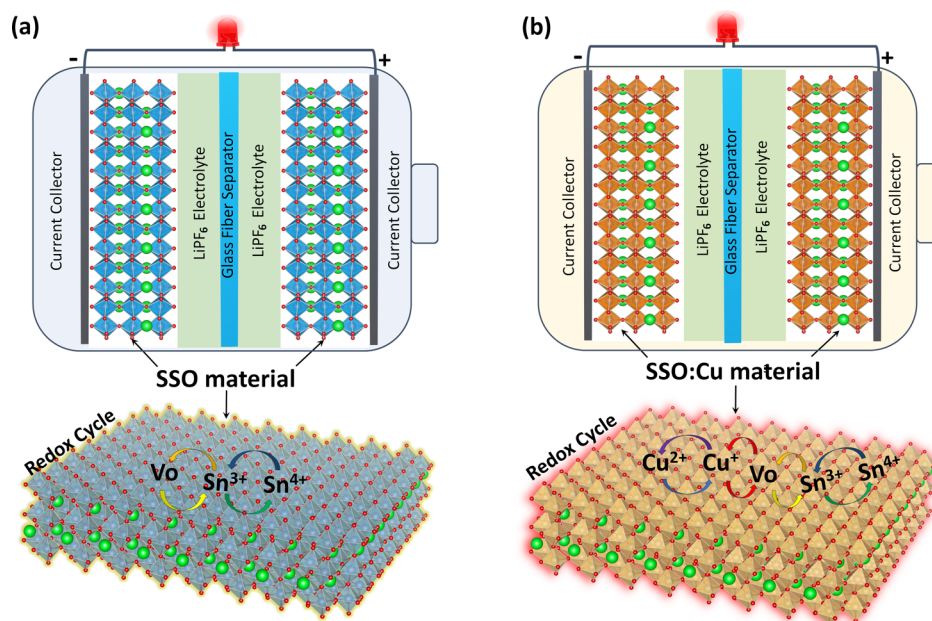
Upon comparing perovskite-based electrodes, while the specific capacitance and energy density are lower than those reported by Elmushyakh and Alqahtani,<sup>20</sup> who used SrSnO<sub>3</sub>/rGO (SSO/rGO) nanohybrid composite material in their work, the power density is substantially higher. The integration of rGO in their work resulted in a significant increase in specific capacitance and energy density. Cao et al.<sup>81</sup> used a

**Table 3.** Comparison between the Performance of Different Perovskites and Other Tin-Based SC Devices and the Best Working SC Based on SSO:Cu2.5<sup>a</sup>

E1	E2	$C_s$ (F g <sup>-1</sup> )	$E_D$ (W h kg <sup>-1</sup> )	$P_D$ (W kg <sup>-1</sup> )	ref
BiFeO <sub>3</sub> :Cu	AC	169	4.71	2.66	80
SrMnO <sub>3</sub> :Ba	AC	423	37.3	400	10
Bi <sub>1-x</sub> Cu <sub>x</sub> FeO <sub>3</sub>	AC	732	37.25	752	33
La <sub>x</sub> Sr <sub>1-x</sub> CoO <sub>3</sub>	AC	747.45	27.7	500	81
SrTiO <sub>3</sub>	symmetric	212.5	27.8	1921	6
SrRuO <sub>3</sub> /rGO	symmetric	160	13.9	78100	82
NiSnO <sub>3</sub>	AC	742	45	1.25	83
FeSnO <sub>3</sub>	AC	2853	45	1.25	83
MnSnO <sub>3</sub>	symmetric	0.1	10	22	19
MnSnO <sub>3</sub> /rGO	symmetric	372			84
SrSnO <sub>3</sub> /rGO	symmetric	1385	66	293	20
SrSn <sub>0.975</sub> Cu <sub>0.025</sub> O <sub>3</sub> (SSO:Cu2.5)	symmetric	613	25.42	32757	this work

<sup>a</sup>E1 and E2, electrodes; AC, activated carbon;  $C_s$ , specific capacity;  $E_D$ , energy density; and  $P_D$ , power density.

Scheme 2. Schematic Diagram for the Designed Symmetric Supercapacitor Devices Based on (a) SSO and (b) SSO:Cu Electrodes, with the Redox Cycle Occurring in the Corresponding Systems



complex system of lanthanum cobaltite nanofibers in combination with activated carbon (AC) to design an asymmetric supercapacitor, and they reported an increase in specific capacitance and energy density. Galal et al.<sup>82</sup> reported a significant increase in power density in their work using a SrRuO<sub>3</sub>/rGO composite structure, with lower specific capacitance and energy density compared to other material systems.

The structure modification of SrSnO<sub>3</sub> by Cu doping herein successfully improved the specific capacitance and energy density without altering the power density to a high degree compared to other perovskite systems, as depicted in Table 3. The mixed valence exchange of tin (Sn<sup>4+</sup>/Sn<sup>3+</sup>) and copper ions (Cu<sup>2+</sup>/Cu<sup>+</sup>) as well as the formation of oxygen vacancies due to the Cu<sup>2+</sup>/Sn<sup>4+</sup> substitution enhanced the charge transfer and mobility in the system. Specifically, capacitive behavior in undoped SSO perovskite was associated with the presence of mixed Sn<sup>4+</sup>/Sn<sup>3+</sup> states and oxygen vacancies. In contrast, the increase of mixed valence cations such as Cu<sup>2+</sup>/Cu<sup>+</sup> and the structural distortions apparently facilitate faster charge diffusion and an enhanced capacitive behavior in Cu-doped SSO systems. Furthermore, the presence of a lower amount of SrCO<sub>3</sub> as a secondary phase minimizes internal resistance, leading to efficient transport throughout the entire electrode/electrolyte interface, and thereby improving the performance of the superconductor. A schematic representation of the designed symmetric supercapacitor devices (SCs) based on the electrode materials of SSO and SSO:Cu perovskites with their corresponding redox-mediated processes is depicted in Scheme 2.

## CONCLUSIONS

SSO and SSO:Cu perovskites were successfully prepared by a modified Pechini method. The samples adopted an orthorhombic distorted *Pbnm* structure after calcination at 900 °C, presenting SrCO<sub>3</sub> as a secondary phase. A lower amount of SrCO<sub>3</sub> present in the SSO doped with 2.5%mol Cu<sup>2+</sup> (SSO:2.5), synergistically with a distorted structure, the

presence of mixed valence cations and oxygen vacancies induced by the doping aligned with the surface charge potential offer more active sites for the electrode–electrolyte interface, resulting in enhanced electrochemical performance and improved specific capacity. Specifically, mixed valence states of Sn<sup>3+</sup>/Sn<sup>4+</sup> in SSO and Cu<sup>+</sup>/Cu<sup>2+</sup> in SSO:Cu<sub>x</sub> samples introduce oxygen vacancies and structural distortion, which improve ionic transport, which in turn boosts the electrochemical performance. Interestingly, a higher amount of SrCO<sub>3</sub> in the samples hinders the rapid ionic charge transport between the electrode–electrolyte interfaces. Symmetric cell devices were constructed with SSO:2.5 as an electrode material, achieving a high energy density of 25.42 W h kg<sup>-1</sup> and a remarkably high-power density of 32,757 W kg<sup>-1</sup>, far superior to other perovskite materials. Therefore, we highlight that SSO:Cu2.5 (SrSn<sub>0.975</sub>Cu<sub>0.025</sub>O<sub>3</sub>) is a new, efficient, and promising perovskite material for applications in the energy storage field.

## ASSOCIATED CONTENT

### Supporting Information

The Supporting Information is available free of charge at <https://pubs.acs.org/doi/10.1021/acs.jpcc.5c03126>.

FTIR spectra, Rietveld refinement data, zeta potential results, UV–vis spectral deconvolution and additional discussion (PDF)

## AUTHOR INFORMATION

### Corresponding Authors

André Luiz Menezes de Oliveira – Núcleo de Pesquisa e Extensão LACOM, Universidade Federal da Paraíba, Pessoa, Paraíba 58051-900, Brazil; Laboratório de Síntese Química de Materiais, Dept. de Engenharia de Materiais, Universidade Federal do Rio Grande do Norte, Natal, Rio Grande do Norte 59078-970, Brazil; [orcid.org/0000-0002-7930-6234](https://orcid.org/0000-0002-7930-6234); Email: [andrel\\_ltm@hotmail.com](mailto:andrel_ltm@hotmail.com)

Arpad Mihai Rostas – National Institute for Isotopic and Molecular Technologies, Cluj-Napoca 400293, Romania; [orcid.org/0000-0001-8190-9512](https://orcid.org/0000-0001-8190-9512); Email: arpad.rostas@itim-cj.ro

Iêda Maria Garcia dos Santos – Núcleo de Pesquisa e Extensão LACOM, Universidade Federal da Paraíba, Pessoa, Paraíba 58051-900, Brazil; [orcid.org/0000-0002-3349-3994](https://orcid.org/0000-0002-3349-3994); Email: ieda@quimica.ufpb.br

## Authors

Adevando Silva – Núcleo de Pesquisa e Extensão LACOM, Universidade Federal da Paraíba, Pessoa, Paraíba 58051-900, Brazil; [orcid.org/0009-0009-2114-7873](https://orcid.org/0009-0009-2114-7873)

Mohamad Hasan Aleinawi – Faculty of Engineering and Natural Sciences, Sabanci University, Tuzla, Istanbul 34956, Turkey

Emre Erdem – Faculty of Engineering and Natural Sciences, Sabanci University, Tuzla, Istanbul 34956, Turkey

Brendan James Kennedy – School of Chemistry, The University of Sydney, Sydney, New South Wales 2006, Australia; [orcid.org/0000-0002-7187-4579](https://orcid.org/0000-0002-7187-4579)

Aurelian Catalin Galca – Laboratory of Complex Heterostructures and Multifunctional Materials (HeCoMat), National Institute of Materials Physics, Magurele 077125, Romania; International Centre for Advanced Training and Research in Physics, Magurele 077125, Romania; [orcid.org/0000-0002-1914-4210](https://orcid.org/0000-0002-1914-4210)

Complete contact information is available at: <https://pubs.acs.org/10.1021/acs.jpcc.5c03126>

## Author Contributions

A.S.: methodology, formal analysis, investigation, visualization, data curation, writing-original draft; M.H.A.: methodology, formal analysis, investigation, visualization, data curation, writing-original draft; E.E.: formal analysis, validation, resources, writing-review and editing; B.J.K.: investigation, formal analysis, validation, resources, writing-review and editing; A.C.G.: investigation, resources, writing-review and editing; I.M.G.S.: methodology, investigation, formal analysis, validation, resources, supervision, funding acquisition, writing-review and editing; A.M.R.: methodology, investigation, formal analysis, data curation, validation, visualization, supervision, funding acquisition, writing-original draft, writing-review and editing; A.L.M.O.: conceptualization, methodology, investigation, formal analysis, data curation, validation, visualization, supervision, funding acquisition, writing-original draft, writing-review and editing.

## Funding

The Article Processing Charge for the publication of this research was funded by the Coordenacao de Aperfeicoamento de Pessoal de Nivel Superior (CAPES), Brazil (ROR identifier: 00x0ma614).

## Notes

The authors declare no competing financial interest.

## ACKNOWLEDGMENTS

The authors acknowledge the financial support of the Brazilian funding agencies—National Council for Scientific and Technological Development, CNPq/MCTIC and Coordination for the Improvement of Higher Education Personnel, CAPES/MEC (finance code 001). A.S. thanks the CAPES, Brazil (grant 88882.440054/2019-01). B.J.K. acknowledges the

support of the Australian Research Council. A.C.G. acknowledges the Core Program of the National Institute of Materials Physics, granted by the Romanian Ministry of Research, Innovation, and Digitalization through Project PC3-PN23080303. A.M.R. acknowledges the support of a grant from the Ministry of Research, Innovation and Digitization, CNCS—UEFISCDI, project number PN-IV-P2-2.1-TE-2023-0048, within PNCEDI IV. A.L.M.O. greatly acknowledges the National Council for Scientific and Technological Development—PDE/CSF/CNPq (grant 232680/2014-0) and PDS/CNPq/MCTI (grant 102504/2024-5), Paraíba State Research Foundation—FAPESQ/PB (grant 008/2022) and National Institute of Materials Physics (project 3SPFE/2021) for the support received to perform his short scientific mission, and also The University of Sydney as well as the Australian Synchrotron.

## REFERENCES

- (1) Cao, Y.; Liang, J.; Li, X.; Yue, L.; Liu, Q.; Lu, S.; Asiri, A. M.; Hu, J.; Luo, Y.; Sun, X. Recent Advances in Perovskite Oxides as Electrode Materials for Supercapacitors. *Chem. Commun.* **2021**, *57*, 2343–2355.
- (2) Shah, S. S.; Niaz, F.; Ehsan, M. A.; Das, H. T.; Younas, M.; Khan, A. S.; Rahman, H. U.; Nayem, S. A.; Oyama, M.; Aziz, M. A. Advanced Strategies in Electrode Engineering and Nanomaterial Modifications for Supercapacitor Performance Enhancement: A Comprehensive Review. *J. Energy Storage* **2024**, *79*, No. 110152.
- (3) Şahin, M. E.; Blaabjerg, F.; Sangwongwanich, A. A Comprehensive Review on Supercapacitor Applications and Developments. *Energies* **2022**, *15*, 674.
- (4) Salleh, N. A.; Kheawhom, S.; Hamid, N. A. A.; Rahiman, W.; Mohamad, A. A. Electrode Polymer Binders for Supercapacitor Applications: A Review. *J. Mater. Res. Technol.* **2023**, *23*, 3470–3491.
- (5) Wilde, P.; Guther, T.; Oesten, R.; Garche, J. Strontium Ruthenate Perovskite as the Active Material for Supercapacitors. *J. Electroanal. Chem.* **1999**, *461*, 154–160.
- (6) Tomar, A. K.; Singh, G.; Sharma, R. K. Charge Storage Characteristics of Mesoporous Strontium Titanate Perovskite Aqueous as well as Flexible Solid-State Supercapacitor Cell. *J. Power Sources* **2019**, *426*, 223–232.
- (7) Joseph, C.; Vinuth Raj, T.; Priya, A. H. *Role of Semiconductors in Future Flexible Batteries. Handbook of Semiconductors: Fundamentals to Emerging Applications*; CRC Press, 2024; ch 24, pp 316–323.
- (8) Hu, Q.; Yue, B.; Shao, H.; Yang, F.; Wang, J.; Wang, Y.; Liu, J. Facile Syntheses of Cerium-Based CeMO<sub>3</sub> (M = Co, Ni, Cu) Perovskite Nanomaterials for High-Performance Supercapacitor Electrodes. *J. Mater. Sci.* **2020**, *55*, 8421–8434.
- (9) Patel, N. K.; Utter, R. G.; Das, D.; Pecht, M. Surface Degradation of Strontium-Based Perovskite Electrodes of Solid Oxide Fuel Cells. *J. Power Sources* **2019**, *438*, No. 227040.
- (10) George, G.; Jackson, S. L.; Luo, C. Q.; Fang, D.; Luo, D.; Hu, D.; Wen, J.; Luo, Z. Effect of Doping on the Performance of High-Crystalline SrMnO<sub>3</sub> Perovskite Nanofibers as a Supercapacitor Electrode. *Ceram. Int.* **2018**, *44*, 21982–21992.
- (11) Lang, X.; Mo, H.; Hu, X.; Tian, H. Supercapacitor Performance of Perovskite La<sub>1-x</sub>Sr<sub>x</sub>MnO<sub>3</sub>. *Dalton Trans.* **2017**, *46*, 13720–13730.
- (12) Meng, D.; Gu, H.; Lu, Q.; Zhao, Y.; Zhu, G.; Zhang, Y.; Zhong, Q.; Bu, Y. Advances and Perspectives for the Application of Perovskite Oxides in Supercapacitors. *Energy Fuels* **2021**, *35*, 17353–17371.
- (13) Qiao, Y.; Liu, G.; Xu, R.; Hu, R.; Liu, L.; Jiang, G.; Demir, M.; Ma, P. SrFe<sub>1-x</sub>LZr<sub>x</sub>O<sub>3-δ</sub> Perovskite Oxides as Negative Electrodes for Supercapacitors. *Electrochim. Acta* **2023**, *437*, No. 141527.
- (14) Zhao, Y.; Li, X.; Yan, B.; Xiong, D.; Li, D.; Lawes, S.; Sun, X. Recent Developments and Understanding of Novel Mixed Transition-Metal Oxides as Anodes in Lithium-Ion Batteries. *Adv. Energy Mater.* **2016**, *6*, No. 1502175.

- (15) Jia, Z.; Cheng, C.; Chen, X.; Liu, L.; Ding, R.; Ye, J.; Wang, J.; Fu, L.; Cheng, Y.; Wu, Y. Applications of All-Inorganic Perovskites for Energy Storage. *Mater. Adv.* **2023**, *4*, 79–104.
- (16) Veerappan, G.; Zhang, K.; Ma, M.; Kang, B.; Park, J. H. High-Reversible Capacity of Perovskite  $BaSnO_3$ /rGO Composite for Lithium-Ion Battery Anodes. *Electrochim. Acta* **2016**, *214*, 31–37.
- (17) Saranya, P.; Selladurai, S. Facile Synthesis of  $NiSnO_3$ /Graphene Nanocomposite for High-Performance Electrode Towards Asymmetric Supercapacitor Device. *J. Mater. Sci.* **2018**, *53*, 16022–16046.
- (18) Wang, Z.; Wang, Z.; Liu, W.; Xiao, W.; Lou, X. W. D. Amorphous  $CoSnO_3$ @C Nanoboxes With Superior Lithium Storage Capability. *Energy Environ. Sci.* **2013**, *6*, 87–91.
- (19) Ghosh, S. K.; Kumari, P.; Singh, H.; Mallick, K. Harnessing Energy on Paper: Symmetric Supercapacitor Based on Manganese Stannate Perovskite Nanoparticles. *J. Alloys Compd.* **2024**, *976*, No. 173178.
- (20) Elmushyakh, A.; Alqahtani, B. Characterization of Manufacturing Material and Carbon Nanohybrid for Renewable Energy and Storage Systems. *J. Energy Storage* **2024**, *92*, No. 112289.
- (21) Chantelle, L.; Menezes de Oliveira, A. L.; Kennedy, B. J.; Maul, J.; da Silva, M. R.; Duarte, T. M.; Albuquerque, A. R.; Sambrano, J. R.; Landers, R.; Siu-Li, M.; et al. Probing the Site-Selective Doping in  $SrSnO_3$ : Eu Oxides and Its Impact on the Crystal and Electronic Structures Using Synchrotron Radiation and DFT Simulations. *Inorg. Chem.* **2020**, *59*, 7666–7680.
- (22) Mohan, T.; Kuppasamy, S.; Michael, R. J. V. Tuning of Structural and Magnetic Properties of  $SrSnO_3$  Nanorods in Fabrication of Blocking Layers for Enhanced Performance of Dye-Sensitized Solar Cells. *ACS Omega* **2022**, *7*, 18531–18541.
- (23) Muthukutty, B.; Karthik, R.; Chen, S.-M.; Abinaya, M. Designing Novel Perovskite-Type Strontium Stannate ( $SrSnO_3$ ) and Its Potential as an Electrode Material for the Enhanced Sensing of Anti-Inflammatory Drug Mesalazine in Biological Samples. *New J. Chem.* **2019**, *43*, 12264–12274.
- (24) Chaganti, V. S. K.; Truttmann, T. K.; Liu, F.; Jalan, B.; Koester, S. J.  $SrSnO_3$  Field-Effect Transistors With Recessed Gate Electrodes. *IEEE Electron Device Lett.* **2020**, *41*, 1428–1431.
- (25) Behera, A.; Seth, D.; Agarwal, M.; Haider, M. A.; Bhattacharyya, A. J. Exploring Cu-Doped  $Co_3O_4$  Bifunctional Oxygen Electrocatalysts for Aqueous Zn–Air Batteries. *ACS Appl. Mater. Interfaces* **2024**, *16*, 17574–17586.
- (26) Nie, C.; Han, G.; Yang, J.; Wang, W.; Zhang, Y.; Kuang, D.; Wu, H. Insight Into Copper Doping Ratio on Optoelectronics Performance of Two-Dimensional Cu-Doped  $SnO_2$  Nanosheets: An Experiment and DFT Study. *ACS Appl. Electron. Mater.* **2023**, *5*, 2422–2432.
- (27) Zhou, X.; Huang, X.; Cui, Y.; Zhu, Y.; Wang, L.; Wang, X.; Tang, S. Cu-Doped Spherical P2-Type  $Na_{0.7}Fe_{0.23-x}Cu_xMn_{0.77}O_2$  Cathode for High-Performance Sodium-Ion Batteries. *ACS Appl. Mater. Interfaces* **2024**, *16*, 36354–36362.
- (28) Wang, J.; Liu, H.; Yang, Q.; Hu, B.; Geng, F.; Zhao, C.; Lin, Y.; Hu, B. Cu-Doped P2- $Na_{0.7}Mn_{0.9}Cu_{0.1}O_2$  Sodium-Ion Battery Cathode With Enhanced Electrochemical Performance: Insight From Water Sensitivity and Surface Mn (II) Formation Studies. *ACS Appl. Mater. Interfaces* **2020**, *12*, 34848–34857.
- (29) Berger, T.; Drexler, H.; Ruh, T.; Lindenthal, L.; Schrenk, F.; Bock, J.; Rameshan, R.; Föttinger, K.; Irrgeher, J.; Rameshan, C. Cu-Doped Perovskite-Type Oxides: A Structural Deep Dive and Examination of Their Exsolution Behaviour Influenced by B-Site Doping. *Catal. Today* **2024**, *437*, No. 114787.
- (30) Zahra, R.; Kumar, A.; Gouadria, S.; Chandra, S.; Sharma, R.; Pathak, P. K.; Chaudhary, R. R.; Mishra, V. Copper Doping in Perovskite Oxide: A Novel Route to High-Performance Oxygen Evolution Reaction. *New J. Chem.* **2025**, *49*, 1773–1785.
- (31) Wang, Y.; Wang, Z.; Wang, D.; Mao, J.; Zhang, C.; Zhang, Y. Revealing the Doping Effect of  $Cu^{2+}$  on  $SrSnO_3$  Perovskite Oxides for  $CO_2$  Electroreduction. *ChemElectroChem* **2022**, *9*, No. e202200635.
- (32) Tezel, F. M.; Güven, F.; Kariper, İ. Production and Characterization of Cu-doped Perovskite Thin Film Electrodes for Supercapacitors. *Inorg. Chem. Commun.* **2022**, *143*, No. 109766.
- (33) Ramadan, A.; Ramadan, W. Superior Performance of Asymmetric Supercapacitor Based on Cu Doped Bismuth Ferrite Electrode. *J. Energy Storage* **2024**, *100*, No. 113702.
- (34) Silva, A.; Hurdley, F.; de Oliveira, A. L. M.; Slater, T.; da Silva Maia, A.; Folli, A.; dos Santos, I. M. G. An EPR Investigation on Reduced Sn Centres in  $SrSnO_3$  Perovskite. *Mater. Lett.* **2024**, *368*, No. 136705.
- (35) Chantelle, L.; de Lima, C. O.; Dantas, M. C.; Siu-Li, M.; Menezes, R. R.; de Souza, F. S.; de Oliveira, A. L. M.; dos Santos, I. M. G.  $Zn_2SnO_4$  and  $Zn_2TiO_4$  Inverse Spinels: Influence of the Temperature on Structural, Microstructural and Luminescent Properties. *J. Therm. Anal. Calorim.* **2024**, *149*, 4453–4468.
- (36) de Oliveira, A. L. M.; Bouquet, V.; Dorcet, V.; Ollivier, S.; Députier, S.; de Souza, A. G.; Siu-Li, M.; Longo, E.; Weber, I. T.; dos Santos, I. M. G.; et al. Evolution of the Structural and Microstructural Characteristics of  $SrSn_{1-x}Ti_xO_3$  Thin Films Under the Influence of the Composition, the Substrate and the Deposition Method. *Surf. Coat. Technol.* **2017**, *313*, 361–373.
- (37) do Nascimento, J. L. A.; Rostas, A. M.; Silva, A.; Kennedy, B. J.; Barbu-Tudoran, L.; Bocirnea, A.-E.; Santos, I. M. G. d.; Alves, M. C. F.; Menezes de Oliveira, A. L. Tailoring Structural Distortions and Ionic Defects as Alternative Strategy to Modulate Reactive Oxygen Species and Photocatalytic Activity in  $SnO_2$  Nanoparticles. *Chem. Mater.* **2025**, 3146.
- (38) De Oliveira, A.; Silva, M.; Sales, H.; Longo, E.; Maia, A.; Souza, A.; Santos, I. Effect of the Composition on the Thermal Behaviour of the  $SSrSn_{1-x}Ti_xO_3$  Precursor Prepared by the Polymeric Precursor Method. *J. Therm. Anal. Calorim.* **2013**, *114*, 565–572.
- (39) Chantelle, L.; Kennedy, B. J.; de Oliveira, C. P.; Gouttefangeas, F.; Siu-Li, M.; Landers, R.; Ciorita, A.; Rostas, A. M.; dos Santos, I. M. G.; de Oliveira, A. L. M. Europium Induced Point Defects in  $SrSnO_3$ -Based Perovskites Employed as Antibacterial Agents. *J. Alloys Compd.* **2023**, *956*, No. 170353.
- (40) Wallwork, K. S.; Kennedy, B. J.; Wang, D. The High Resolution Powder Diffraction Beamline for the Australian Synchrotron. *AIP Conf. Proc.* **2007**, *879*, 879–882.
- (41) Toby, B. H.; Von Dreele, R. B. GSAS-II: The Genesis of a Modern Open-Source All-Purpose Crystallography Software Package. *J. Appl. Crystallogr.* **2013**, *46*, 544–549.
- (42) Cowie, B.; Tadich, A.; Thomsen, L. The Current Performance of the Wide Range (90–2500 eV) Soft X-ray Beamline at the Australian Synchrotron. *AIP Conf. Proc.* **2010**, *1234*, 307–310.
- (43) Ravel, B.; Newville, M.; Athena, A. HEPHAESTUS: Data Analysis for X-ray Absorption Spectroscopy Using IFFFIT. *J. Synchrotr. Radiat.* **2005**, *12*, 537–541.
- (44) Green, M.; Prassides, K.; Day, P.; Neumann, D. Structure of the  $n=2$  and  $n=\infty$  Member of the Ruddlesden-Popper Series,  $Sr_{n+1}SnO_{3n+1}$ . *Int. J. Inorg. Mater.* **2000**, *2*, 35–41.
- (45) Melo, D.; Marinho, R.; Vieira, F.; Lima, S.; Longo, E.; Souza, A.; Maia, A.; Santos, I. Influence of Cu(II) in the  $SrSnO_3$  Crystallization. *J. Therm. Anal. Calorim.* **2011**, *106*, 513–517.
- (46) Aidhy, D. S.; Liu, B.; Zhang, Y.; Weber, W. J. Chemical Expansion Affected Oxygen Vacancy Stability in Different Oxide Structures from First Principles Calculations. *Comput. Mater. Sci.* **2015**, *99*, 298–305.
- (47) Vieira, F.; Oliveira, A.; Melo, D.; Lima, S.; Longo, E.; Maia, A.; Souza, A.; Santos, I. Crystallization Study of  $SrSnO_3$ :Fe. *J. Therm. Anal. Calorim.* **2011**, *106*, 507–512.
- (48) Robinson, K.; Gibbs, G.; Ribbe, P. Quadratic Elongation: A Quantitative Measure of Distortion in Coordination Polyhedra. *Science* **1971**, *172*, 567–570.
- (49) Maul, J.; Dos Santos, I. M. G.; Sambrano, J. R.; Casassa, S.; Erba, A. A Quantum-Mechanical Investigation of Oxygen Vacancies and Copper Doping in the Orthorhombic  $CaSnO_3$  perovskite. *Phys. Chem. Chem. Phys.* **2018**, *20*, 20970–20980.

- (50) Gurevich, A. B.; Bent, B. E.; Teplyakov, A. V.; Chen, J. G. A NEXAFS Investigation of the Formation and Decomposition of CuO and Cu<sub>2</sub>O Thin Films on Cu (100). *Surf. Sci.* **1999**, *442*, L971–L976.
- (51) Sharma, A.; Varshney, M.; Park, J.; Ha, T.-K.; Chae, K.-H.; Shin, H.-J. XANES, EXAFS and Photocatalytic Investigations on Copper Oxide Nanoparticles and Nanocomposites. *RSC Adv.* **2015**, *5*, 21762–21771.
- (52) Sharma, A.; Varshney, M.; Ha, T.-K.; Chae, K.-H.; Shin, H.-J. X-ray Absorption Spectroscopy Study and Photocatalyst Application of CuO and Cu<sub>0.5</sub>Ti<sub>0.1</sub>O Nanoparticles. *Curr. Appl. Phys.* **2015**, *15*, 1148–1155.
- (53) Asokan, K.; Jan, J.; Chiou, J.; Pong, W.; Tsai, M.-H.; Chang, Y.; Chen, Y.; Hsieh, H.; Lin, H.-J.; Yang, Y.; et al. The Electronic Structure of Ba<sub>1-x</sub>Ca<sub>x</sub>TiO<sub>3</sub> Probed by X-ray Absorption Spectroscopy. *J. Solid State Chem.* **2004**, *177*, 2639–2643.
- (54) Sharma, A.; Varshney, M.; Shin, H. J.; Chae, K. H.; Won, S. O. X-ray Absorption Spectroscopy Investigations on Electronic Structure and Luminescence Properties of Eu:SnO<sub>2</sub>-SnO Nanocomposites. *Curr. Appl. Phys.* **2016**, *16*, 1342–1348.
- (55) Muralidharan, M.; Thiagarajan, R.; Sivakumar, K.; Sivaji, K. Near Infrared Emission and Enhanced Ferromagnetism in Fe-Doped SrSnO<sub>3</sub> Perovskite Structured Nanorods. *J. Mater. Sci.: Mater. Electron.* **2019**, *30*, 4634–4643.
- (56) Ong, K. P.; Fan, X.; Subedi, A.; Sullivan, M. B.; Singh, D. J. Transparent Conducting Properties of SrSnO<sub>3</sub> and ZnSnO<sub>3</sub>. *APL Mater.* **2015**, *3*, No. 062505.
- (57) Saran Kumar Chaganti, V.; Golani, P.; Truttman, T. K.; Liu, F.; Jalan, B.; Koester, S. J. Optimizing Ohmic Contacts to n-Doped n-Type SrSnO<sub>3</sub>Nd. *Appl. Phys. Lett.* **2021**, *118*, 142104.
- (58) Gao, Q.; Chen, H.; Li, K.; Liu, Q. Band Gap Engineering and Room-Temperature Ferromagnetism by Oxygen Vacancies in SrSnO<sub>3</sub> Epitaxial Films. *ACS Appl. Mater. Interfaces* **2018**, *10*, 27503–27509.
- (59) Wood, D.; Tauc, J. Weak Absorption Tails in Amorphous Semiconductors. *Phys. Rev. B* **1972**, *5*, 3144.
- (60) Honorio, L. M. C.; de Oliveira, A. L. M.; da Silva Filho, E. C.; Osajima, J. A.; Hakki, A.; Macphée, D. E.; dos Santos, I. M. G. Supporting the Photocatalysts on ZrO<sub>2</sub>: An Effective Way to Enhance the Photocatalytic Activity of SrSnO<sub>3</sub>. *Appl. Surf. Sci.* **2020**, *528*, No. 146991.
- (61) Zheng, T.; Deng, H.; Zhou, W.; Zhai, X.; Cao, H.; Yu, L.; Yang, P.; Chu, J. Bandgap Modulation and Magnetic Switching in PbTiO<sub>3</sub> Ferroelectrics by Transition Elements Doping. *Ceram. Int.* **2016**, *42*, 6033–6038.
- (62) Lee, C. W.; Kim, D. W.; Cho, I. S.; Park, S.; Shin, S. S.; Seo, S. W.; Hong, K. S. Simple Synthesis and Characterization of SrSnO<sub>3</sub> Nanoparticles With Enhanced Photocatalytic Activity. *Int. J. Hydrogen Energy* **2012**, *37*, 10557–10563.
- (63) Alammari, T.; Slowing, I. I.; Anderegg, J.; Mudring, A.-V. Ionic-Liquid-Assisted Microwave Synthesis of Solid Solutions of Sr<sub>1-x</sub>Ba<sub>x</sub>SnO<sub>3</sub> Perovskite for Photocatalytic Applications. *ChemSusChem* **2017**, *10*, 3387–3401.
- (64) Mizoguchi, H.; Eng, H. W.; Woodward, P. M. Probing the Electronic Structures of Ternary Perovskite and Pyrochlore Oxides Containing Sn<sup>4+</sup> or Sb<sup>5+</sup>. *Inorg. Chem.* **2004**, *43*, 1667–1680.
- (65) Schumann, T.; Raghavan, S.; Ahadi, K.; Kim, H.; Stemmer, S. Structure and Optical Band Gaps of (Ba, Sr)SnO<sub>3</sub> Films Grown by Molecular Beam Epitaxy. *J. Vac. Sci. Technol. A* **2016**, *34*, No. 050601.
- (66) Bera, M.; Kaur, S.; Keshari, K.; Santra, A.; Moonshiram, D.; Paria, S. Structural and Spectroscopic Characterization of Copper (III) Complexes and Subsequent One-Electron Oxidation Reaction and Reactivity Studies. *Inorg. Chem.* **2023**, *62*, 5387–5399.
- (67) Rada, S.; Unguresan, M.; Rada, M.; Tudoran, C.; Wang, J.; Culea, E. Performance of the Recycled and Copper-Doped Materials from Spent Electrodes by XPS and Voltammetric Characteristics. *J. Electrochem. Soc.* **2020**, *167*, No. 090548.
- (68) Stevic, N.; Korac, J.; Pavlovic, J.; Nikolic, M. Binding of Transition Metals to Monosilicic Acid in Aqueous and Xylem (*Cucumis sativus* L.) Solutions: A Low-T Electron Paramagnetic Resonance Study. *Biometals* **2016**, *29*, 945–951.
- (69) Stefan, M.; Rostas, A. M.; Ammar, A. U.; Gungor, A.; Saritas, E.; Toloman, D.; Varadi, A.; Macavei, S.; Barbu-Tudoran, L.; Leostean, C.; et al. Cerium Enhanced Supercapacitive Properties of Zinc Oxide Nanoflowers. *Energy Fuels* **2024**, *38*, 19088–19099.
- (70) Tuc Altaf, C.; Rostas, A. M.; Popa, A.; Toloman, D.; Stefan, M.; Demirci Sankir, N.; Sankir, M. Recent Advances in Photochargeable Integrated and All-in-One Supercapacitor Devices. *ACS Omega* **2023**, *8*, 47393–47411.
- (71) Ammar, A. U.; Stan, M.; Popa, A.; Toloman, D.; Macavei, S.; Leostean, C.; Ciorita, A.; Erdem, E.; Rostas, A. M. All-in-One Supercapacitor Devices Based on Nanosized Mn<sup>4+</sup>-Doped WO<sub>3</sub>. *J. Energy Storage* **2023**, *72*, No. 108599.
- (72) Aleinawi, M. H.; Saritas, E.; Stefan, M.; Ammar, A. U.; Hroub, A.; Misirlioglu, F. B.; Bocirnea, A.; Macavei, S.; Tripon, S.; Erdem, E.; Rostas, A. M. Supercapacitor Devices Based on Multiphase MgTiO<sub>3</sub> Perovskites Doped With Mn<sup>2+</sup> Ions. *Mater. Chem. Phys.* **2025**, *329*, No. 130016.
- (73) Wang, J.; Polleux, J.; Lim, J.; Dunn, B. Pseudocapacitive Contributions to Electrochemical Energy Storage in TiO<sub>2</sub> (Anatase) Nanoparticles. *J. Phys. Chem. C* **2007**, *111*, 14925–14931.
- (74) Shao, Y.; El-Kady, M. F.; Sun, J.; Li, Y.; Zhang, Q.; Zhu, M.; Wang, H.; Dunn, B.; Kaner, R. B. Design and Mechanisms of Asymmetric Supercapacitors. *Chem. Rev.* **2018**, *118*, 9233–9280.
- (75) Choi, C.; Ashby, D. S.; Butts, D. M.; DeBlock, R. H.; Wei, Q.; Lau, J.; Dunn, B. Achieving High Energy Density and High Power Density With Pseudocapacitive Materials. *Nat. Rev. Mater.* **2020**, *5*, 5–19.
- (76) Ranjan, B.; Kaur, D. Pseudocapacitive Kinetics in Synergistically Coupled MoS<sub>2</sub>-Mo<sub>2</sub>N Nanowires with Enhanced Interfaces toward All-Solid-State Flexible Supercapacitors. *ACS Appl. Mater. Interfaces* **2024**, *16*, 14890–14901.
- (77) Raavi, R.; Archana, S.; Reddy, P. A.; Elumalai, P. Performances of Dual Carbon Multi-Ion Supercapacitors in Aqueous and Non-Aqueous Electrolytes. *Energy Adv.* **2023**, *2*, 385–397.
- (78) Zhang, Y.; Hu, S.; Chen, P.-Y.; Zhu, J.; Chen, B.; Bai, R.; Zhu, H.; Chen, L.; Zhang, D. W.; Lee, J. C.; et al. Post-Annealing Optimization of the Heteroepitaxial La-Doped SrSnO<sub>3</sub> Integrated on Silicon Via ALD. *Nanoscale* **2023**, *15*, 9432–9439.
- (79) Sharma, M.; Gaur, A. Cu Doped Zinc Cobalt Oxide Based Solid-State Symmetric Supercapacitors: A Promising Key for High Energy Density. *J. Phys. Chem. C* **2020**, *124*, 9–16.
- (80) Tanapongpisit, N.; Wongprasod, S.; Laohana, P.; Sonsupap, S.; Khajonrit, J.; Musikajaroen, S.; Wongprat, U.; Yotburut, B.; Maensiri, S.; Meevasana, W.; Saenrang, W. Enhancing Activated Carbon Supercapacitor Electrodes Using Sputtered Cu-Doped BiFeO<sub>3</sub> Thin Films. *Sci. Rep.* **2024**, *14*, 27811.
- (81) Cao, Y.; Lin, B.; Sun, Y.; Yang, H.; Zhang, X. Symmetric/Asymmetric Supercapacitor Based on the Perovskite-Type Lanthanum Cobaltate Nanofibers With Sr-Substitution. *Electrochim. Acta* **2015**, *178*, 398–406.
- (82) Galal, A.; Hassan, H. K.; Jacob, T.; Atta, N. F. Enhancing the Specific Capacitance of SrRuO<sub>3</sub> and Reduced Graphene Oxide in NaNO<sub>3</sub>, H<sub>3</sub>PO<sub>4</sub> and KOH Electrolytes. *Electrochim. Acta* **2018**, *260*, 738–747.
- (83) Padha, B.; Verma, S.; Arya, S. Fabric-Based Wearable Self-Powered Asymmetric Supercapacitor Comprising Lead-Free Perovskite Piezoelectrodes. *Adv. Mater. Technol.* **2022**, *7*, No. 2200079.
- (84) Liu, P.; Hao, Q.; Xia, X.; Lei, W.; Xia, H.; Chen, Z.; Wang, X. Hollow Amorphous MnSnO<sub>3</sub> Nanohybrid With Nitrogen-Doped Graphene for High-Performance Lithium Storage. *Electrochim. Acta* **2016**, *214*, 1–10.